

❸ A Numerical Study on Rapid Intensification of Typhoon Vicente (2012) in the South China Sea. Part I: Verification of Simulation, Storm-Scale Evolution, and Environmental Contribution

XIAOMIN CHEN

Key Laboratory for Mesoscale Severe Weather/MOE and School of Atmospheric Sciences, Nanjing University, Nanjing, China, and International Pacific Research Center, and Department of Atmospheric Sciences, School of Ocean and Earth Science and Technology, University of Hawai'i at Mānoa, Honolulu, Hawaii

YUQING WANG

International Pacific Research Center, and Department of Atmospheric Sciences, School of Ocean and Earth Science and Technology, University of Hawai'i at Mānoa, Honolulu, Hawaii

KUN ZHAO

Key Laboratory for Mesoscale Severe Weather/MOE and School of Atmospheric Sciences, Nanjing University, Nanjing, China

DAN WU

Shanghai Typhoon Institute, China Meteorological Administration, Shanghai, China

(Manuscript received 14 April 2016, in final form 3 December 2016)

ABSTRACT

Typhoon Vicente (2012) underwent an extreme rapid intensification (RI) over the northern South China Sea just before its landfall in south China. The extreme RI, the sudden track deflection, and the inner- and outer-core structures of Vicente were reasonably reproduced in an Advanced Research version of the Weather Research and Forecasting (WRF-ARW) Model simulation. The evolutions of the axisymmetric inner-core radar reflectivity and the primary circulation of the simulated Vicente before its landfall were verified against the Doppler radar observations.

Two intensification stages were identified: 1) the asymmetric intensification stage (i.e., RI onset), represented by a relatively slow intensification rate accompanied by a distinct eyewall contraction; and 2) the axisymmetric RI stage with very slow eyewall contraction. Results from a storm-scale tangential wind tendency budget indicated that the primary spinup mechanism during the first stage was the radial eddy momentum transport, which was beneficial to accelerate primary circulation inside the radius of maximum wind (RMW) and thus conducive to eyewall contraction. In contrast, the principal spinup mechanism during the second stage was mainly ascribed to the forced secondary circulation in response to diabatic heating in the eyewall and boundary layer friction, which efficiently transported the absolute angular momentum radially inward and vertically upward to increase the primary circulation in the eyewall region throughout the troposphere. Further analysis revealed that the interaction between the monsoon circulation and storm-scale vorticity anomalies played an important role in erecting the tilted vortex and spinning up the midtropospheric TC circulation during the first stage.

1. Introduction

❸ Denotes content that is immediately available upon publication as open access.

Compared with the track forecasts, our ability to forecast tropical cyclone (TC) intensity change, especially rapid intensification (RI), is very limited (Elsberry et al.

Corresponding author e-mail: Yuqing Wang, yuqing@hawaii.edu

2007; DeMaria et al. 2014). The RI is often defined as the maximum sustained 10-m wind increase over 15.4 m s^{-1} in 24 h in many previous studies (Kaplan and DeMaria 2003; Stevenson et al. 2014; Reasor et al. 2009; Chen and Zhang 2013; Zhang and Tao 2013). Statistical analyses indicate that RI often occurs in the environment with high SST, low vertical wind shear (VWS), a moist mid- to lower troposphere, and favorable forcing from the upper-level trough (Kaplan and DeMaria 2003; Kaplan et al. 2010; Shu et al. 2012; Chen et al. 2015).

Earlier understanding on TC RI was primarily based on axisymmetric dynamics. In the classic axisymmetric viewpoint, TC intensification can be attributed to the positive feedback between the primary and secondary circulations. This positive feedback can be described by the Sawyer-Eliassen equation for the transverse circulation in a gradient and hydrostatic balanced axisymmetric vortex in response to diabatic heating in the eyewall (Shapiro and Willoughby 1982; Schubert and Hack 1982; Pendergrass and Willoughby 2009). Diabatic heating in the eyewall drives inflow in the lower troposphere, which brings large absolute angular momentum (AAM) inward, leading to the spinup of the primary circulation (tangential wind) and thus the intensification of the TC vortex. The intensified primary circulation increases the inner-core inertial stability and thus the heating efficiency for the formation of the warm core structure and in turn the spinup of the primary circulation. This positive feedback has been articulated to explain the dependence of RI on TC intensity and inner-core size in observations (Xu and Wang 2015).

More recent studies have focused on the asymmetric spinup process, in particular during the weak stage of a TC. For example, results from idealized numerical experiments (Montgomery and Kallenbach 1997; Enagonio and Montgomery 2001; Möller and Montgomery 2000) and observational studies (e.g., Molinari et al. 2006; Nguyen and Molinari 2015) have shown that the asymmetric eddies in the inner-core region can spin up a TC-like vortex through the wave-mean flow interaction and axisymmetrization process. One potential mechanism for asymmetric intensification comes from the convective-scale forcing, such as the vortical hot towers (VHTs) by Hendricks et al. (2004) and further elaborated by Montgomery et al. (2006). By the asymmetric spinup mechanism associated with VHTs, TC intensification can be viewed as a consequence of the merging of VHT-induced small-scale vorticity patches, the moistening of the midtroposphere due to convective activity, the axisymmetrization of the asymmetric vorticity anomalies, and the collective heating in the VHTs, which forces the transverse circulation and thus the spinup of storm-scale circulation.

Although asymmetric, loosely organized convective eddies, such as VHTs, can form in weak TCs; large

systematic asymmetries can often be forced by environmental VWS (Jones 1995; Wang and Holland 1996; Frank and Ritchie 1999, 2001; Reasor et al. 2004; Heymsfield et al. 2006; Xu and Wang 2013). Although VWS is commonly considered a detrimental effect on TC intensification and intensity (Gray 1968; Tang and Emanuel 2010; Riemer et al. 2010; Zeng et al. 2010; Wang et al. 2015), some studies (Molinari et al. 2004, 2006; Molinari and Vollaro 2010b; Nguyen and Molinari 2012, 2015) have revealed that environmental VWS can serve as a trigger for RI in some TC cases [e.g., Tropical Storm Gabrielle (2001), Hurricane Danny (2004), and Hurricane Irene (1999)]. These studies have demonstrated that if the shear-induced downshear convective activity is sufficiently strong with convective heating occurring within the radius of maximum wind (RMW), a new circulation center may form under the strong convection and the TC could intensify and even intensify rapidly if a vertical alignment of the storm-scale circulation occurs.

In addition to the storm-scale dynamics, asymmetric convective forcing, and the effect of environmental VWS, summer monsoon circulation over the western North Pacific (WNP) and South China Sea (SCS) may contribute to TC genesis and intensification through complex multiscale interactions (Holland 1995; Ritchie and Holland 1997). As indicated by Ritchie and Holland (1999), the monsoon trough is one of the most important large-scale environmental systems, which gives birth to 70%–80% of all TCs in the WNP (see also Molinari and Vollaro 2013). Based on a statistical analysis, recently Chen et al. (2015) identified six low-level flow patterns favorable for TC RI as well as significant environmental factors discriminating RI and non-RI cases over the SCS. They showed that RI TCs in the SCS are generally embedded in the monsoon environment with the provision of a low-level monsoon jet, favorable upper-level forcing [i.e. relative eddy angular momentum flux convergence (REFC)], and low environmental VWS. Because of their climatological and synoptic focus, Chen et al. (2015) have not investigated the detailed dynamical and thermodynamic processes responsible for each of the RI flow patterns. Understanding the multiscale interaction during RI of TCs over the SCS is both scientifically and practically important. This is mainly because RI TCs in the SCS typically make landfall within 1–2 days after their RI phase, thus posing a very challenging issue for operational forecasts.

Typhoon Vicente (2012) formed over the SCS and underwent an extreme RI [i.e., an estimated 65-kt (33.4 m s^{-1}) increase in its maximum sustained 10-m wind speed within 15 h] in the northern SCS just prior to its landfall near Pearl River Delta region of Guangdong Province, China, according to the best track data of the Joint Typhoon Warning Center (JTWC). It was ranked among the

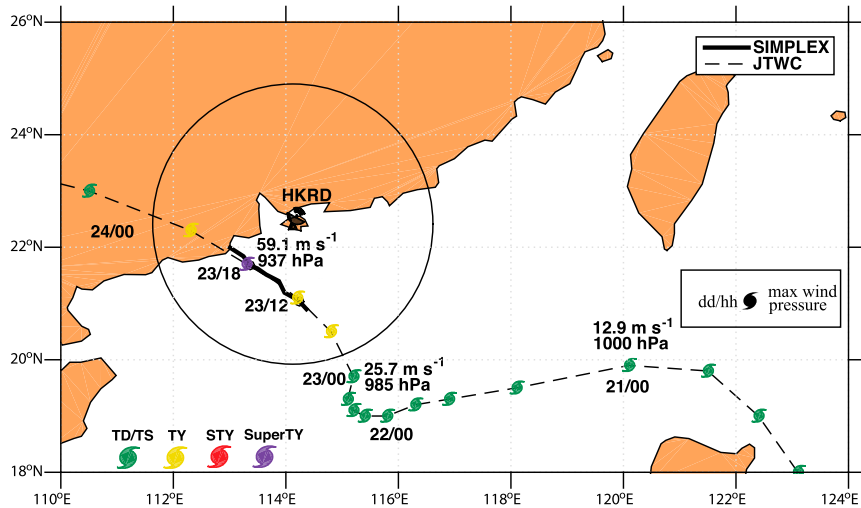


FIG. 1. The 6-hourly JTWC best track (dashed black line) for Typhoon Vicente (2012) from 0600 UTC 20 Jul to 0600 UTC 24 Jul. Different colors of the typhoon symbols denote different TC intensity, ranging from TD/TS to typhoon (TY), severe TY (STY), and super TY according to the CMA TC intensity scaling (bottom-left corner). The maximum 10-m sustained wind and pressure at 0000 and 1800 UTC 23 Jul are shown as well. The half-hourly “GBVTD-simplex” circulation centers based on HIRDLS (black radar symbol) observation from 0800 to 2030 UTC 23 Jul are overlaid as a thick black line. The circle centered on HIRDLS with a radius of 256 km denotes the range of detectable Doppler velocity.

strongest typhoons that affected this area and was responsible for a direct economic loss of about \$370 million (U.S. dollars) for the three onshore provinces in south China according to the *Yearbook of Tropical Cyclones* [China Meteorological Administration (CMA) 2012]. Neither global nor regional models of different forecast agencies captured the extreme RI and the accompanied abrupt track deflection of Vicente, making it an appealing case being studied in recent years (e.g., Shieh et al. 2013; Li et al. 2014). Shieh et al. (2013) attributed the extreme RI of Vicente to the propagation of an upper-tropospheric “inverted” trough while Li et al. (2014) speculated that the convective bursts injected into the storm core was the major cause of RI. However, the detailed mechanisms responsible for the RI of Vicente, in particular the multi-scale interaction processes associated with the RI onset, have not been investigated.

Given the fact that Typhoon Vicente experienced its RI in the SCS monsoon environment that is rich in moisture and background vorticity, one of our major objectives of this study is to understand the contribution of monsoon environment to the RI onset. In addition, whether the upper-level trough mentioned earlier played a significant role in Vicente’s RI will be also investigated. In Part I, both the asymmetric and axisymmetric intensification processes will be examined and the environmental contribution to the RI onset will be further evaluated based on the analysis of a finescale,

cloud-resolving simulation. The rest of the paper is organized as follows. A brief overview of Typhoon Vicente and the associated large-scale environmental conditions will be given in section 2. The model setup and verification of a control simulation against multiplatform remote sensing observations will be discussed in section 3. The storm-scale evolution during two RI stages and the mechanisms in terms of the storm-scale processes responsible for each of the RI stages will be analyzed in sections 4 and 5, respectively. In section 6, the environmental contribution to the RI onset, including the monsoon trough and upper-tropospheric trough, will be examined. Major results will be summarized in the last section.

2. An overview of Typhoon Vicente (2012)

Typhoon Vicente formed as a tropical disturbance in the monsoon trough east of Luzon Island, Philippines, on 18 July 2012. It intensified gradually in the south-easterly steering flow to the south of the WNP subtropical ridge and entered the SCS on 21 July as a tropical depression. After 22 July, the westward motion of Vicente decelerated and the track exhibited an abrupt northward turning. The extreme RI commenced immediately after the track deflection. Vicente intensified from 25.7 m s^{-1} at 0000 UTC 23 July to 59.1 m s^{-1} , as a supertyphoon, at 1800 UTC 23 July (Fig. 1). Two hours later, it made landfall in Taizhou, Guangdong Province

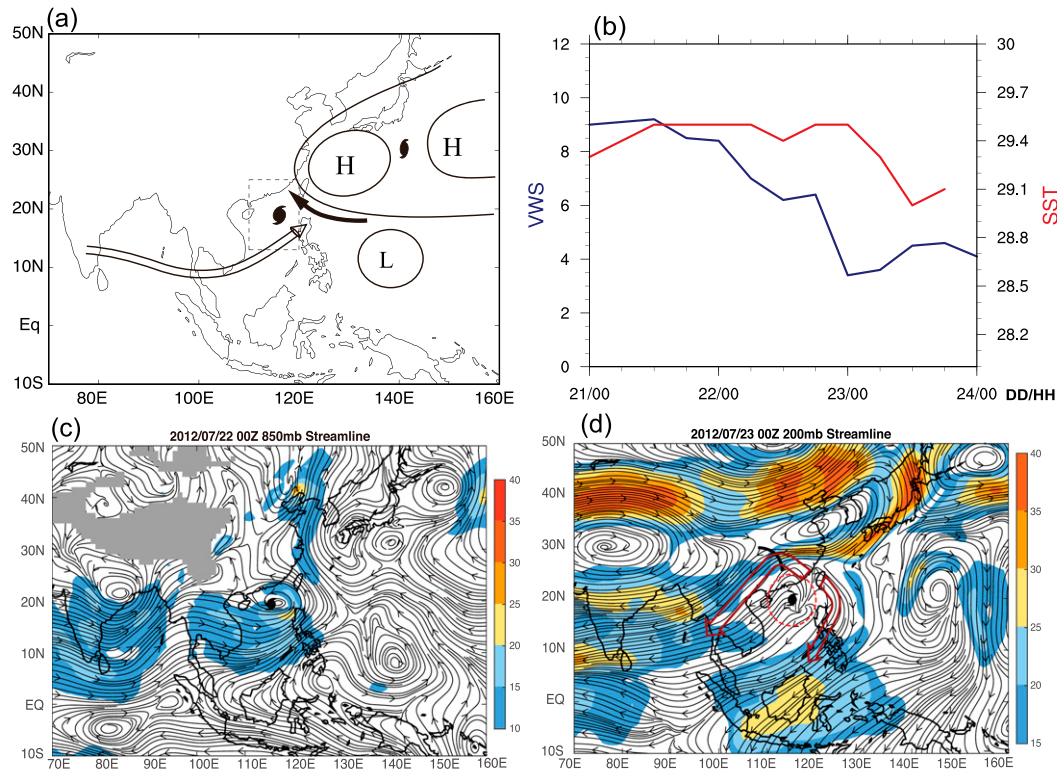


FIG. 2. (a) Low-level RI flow pattern SU1 [cf. Fig. 4f in Chen et al. (2015)]. (b) Time series of 300–850-hPa vertical wind shear (m s^{-1}) averaged between 300- and 800-km radii from the storm center and sea surface temperature ($^{\circ}\text{C}$) averaged within a radius of 1° from 21 to 24 Jul 2012. (c) The 850-hPa flow pattern at 0000 UTC 22 Jul. (d) The 200-hPa flow pattern at 0000 UTC 23 Jul. The shading in (c),(d) represents the ground-relative wind magnitude (m s^{-1}). The 500-km radii centered on TC center is marked as a red circle in (d) and the black curve represents the upper-tropospheric trough line. The thick red arrows represent the outflow channel.

in south China. As Vicente was in the surveillance range (256 km) of Hong Kong Doppler radar (HKRD) from 0800 UTC 23 July to its landfall at 2000 UTC 23 July (Fig. 1), its inner-core region has been well captured by HKRD. The track based on the low-level “GBVTD-simplex”¹ TC center derived from the single Doppler radar observations was also shown in Fig. 1, which was very similar to that from the JTWC best track.

The low-level environmental flow pattern 24 h prior to the onset of RI (Fig. 2c) fits well the RI flow pattern SU1² (Fig. 2a). Climatologically, VWS over the SCS is typically stronger in the summer monsoon season than in the pre-monsoon and postmonsoon seasons, and therefore very

few TCs experience RI in summer season. It is worthwhile to note that SU1 is the only RI flow pattern in the summer monsoon season in SCS. It is characterized by the existence of a low-level monsoon jet and a westward shift of the subtropical high, both enhancing the moisture and momentum transport to the TC circulation and favorable for TC intensification. In the upper troposphere, two outflow channels, one westward and one equatorward, were established at 0000 UTC 23 July (Fig. 2d), giving rise to a strong divergent flow pattern. The westward propagation of the inverted trough and the poleward convective ridging alleviated the previously prevailing easterly wind and was responsible for the rapid shrinking of environmental VWS just prior to RI (6.4 m s^{-1} at 1800 UTC 22 July to 3.4 m s^{-1} at 0000 UTC 23 July) as shown in Fig. 2b. The upper-level outflow channels could also accelerate the removal of the upper-level mass field and thus strengthen the secondary (in-up-out) circulation, enhancing the TC primary circulation. In addition, Vicente stayed over the warm SCS with sea surface temperature (SST) over 29°C even though the SST decreased slightly after 0000 UTC 23 July. The upper-tropospheric inverted

¹ The GBVTD-simplex method was proposed by Lee and Marks (2000) to objectively estimate the TC center by maximizing the retrieved azimuthal mean tangential wind using the Doppler velocity datasets. It can estimate the TC center within 2 km of the actual center for a real TC.

² SU1 represents the RI flow pattern in the summer monsoon season in the SCS [see Fig. 4f in Chen et al. (2015)]. It is identified based on the all RI TCs in the SCS during 1981–2011.

trough near 25°N was located approximately 500 km away from the TC center prior to and during the RI episode. There was no significant interaction that occurred between the upper-level trough and the TC circulation based on the definition in DeMaria et al. (1993), because the REFC at 200 hPa within the 300–600-km radii was less than $10 \text{ m s}^{-1} \text{ day}^{-1}$ (not shown).

In this following analysis, we will focus on contributions by the storm-scale processes and the large-scale environment to the RI based on a successful numerical simulation of Vicente using the Advanced Research version of the Weather Research and Forecasting (WRF-ARW) Model as described in the next section. The mesoscale and convective scale processes will be discussed in Part II.

3. Model setup and verification of simulation

a. Model setup

The WRF-ARW Model, version 3.3.1 (hereafter WRF, Skamarock et al. 2008), was employed to simulate the RI of Typhoon Vicente. The model domain was two-way interactive, triply nested with horizontal resolutions of 18, 6, and 2 km, respectively (Fig. 3). The dimensions of the three meshes were 366×273 , 291×291 , and 330×330 , respectively. The outer two meshes were initiated at 0000 UTC 21 July and run for 72 h while the innermost mesh was activated 36 h later (i.e., 1200 UTC 22 July), and ended at the same time as the outer two meshes. The outermost 18-km mesh was stationary while the inner two meshes automatically moved to follow the model TC. The model had 28 uneven sigma levels extending from the surface to the top at 50 hPa. The European Centre for Medium-Range Weather Forecasts interim reanalysis (ERA-Interim) data were used for initial and lateral boundary conditions. The National Oceanic and Atmospheric Administration (NOAA) daily optimally interpolated SST (OISST) data with 0.25×0.25 resolution were used as the lower boundary condition and were updated daily during the model integration.

The following physics parameterizations were used in this study: the Kain–Fritsch cumulus parameterization scheme (Kain and Fritsch 1993) in the outermost 18-km mesh, the Goddard microphysics scheme (Tao and Simpson 1993), the Yonsei University scheme for planetary boundary layer (Noh et al. 2003), the Dudhia shortwave radiation (Dudhia 1989), and the Rapid Radiative Transfer Model (RRTM) longwave radiation scheme (Mlawer et al. 1997). The same physical parameterization schemes were applied to all three meshes except for the cumulus parameterization scheme. The spectral large-scale nudging toward the reanalysis data (driving field) was applied to the outermost mesh during the

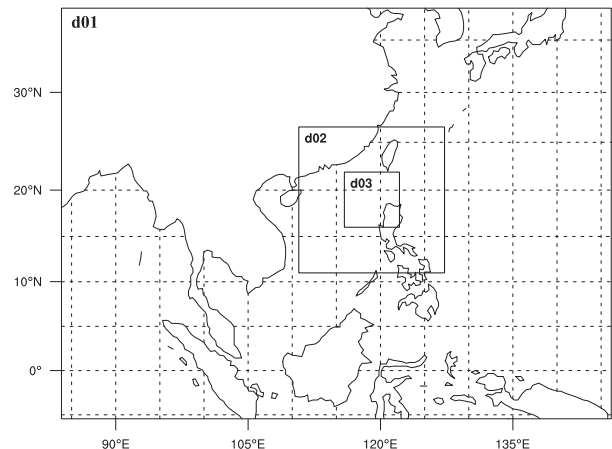


FIG. 3. Triply nested domain settings used for the Typhoon Vicente (2012) simulation.

model integration to reduce biases in the large-scale environmental field and to improve the storm-track simulation (Wang and Wang 2014).

The TC center in the following analysis was defined as the centroid of sea level pressure (Wang 2007), which could represent the storm center well, especially for weak TCs (Nguyen et al. 2014). The model outputs were given at every 10 min for budget analyses. To separate the environment and TC circulation fields, the two-dimensional fast Fourier transfer (FFT) method was adopted, which can separate different scales of motion reasonably well (e.g., Fang and Zhang 2010).

b. Verification of simulation

The simulation successfully reproduced the RI in terms of the minimum sea level pressure (SLP) and maximum 10-m wind speed (VMAX), and the sudden northward track deflection of Typhoon Vicente (Figs. 4a–c). The VMAX oscillation during 1500 UTC 22 July–0300 UTC 23 July was due to the mesovortex activity within the inner-core region. The model also captured nicely the timing and location of landfall as well as the following rapid weakening after landfall. Nevertheless, the simulated track showed some northward deviations in the first 36-h integration. This phenomenon could be partially attributed to the TC center definition (i.e., pressure centroid) used in our study, which is not very sensitive to the downshear convective activities. Note that the track difference among three different agencies [CMA, JTWC, and the Japan Meteorological Agency (JMA)] was considerably large as well during this period, indicating that large uncertainties existed in determining the storm center at its weak stage from observations.

The model captured both magnitude and direction of the environmental VWS between 300 and 850 hPa

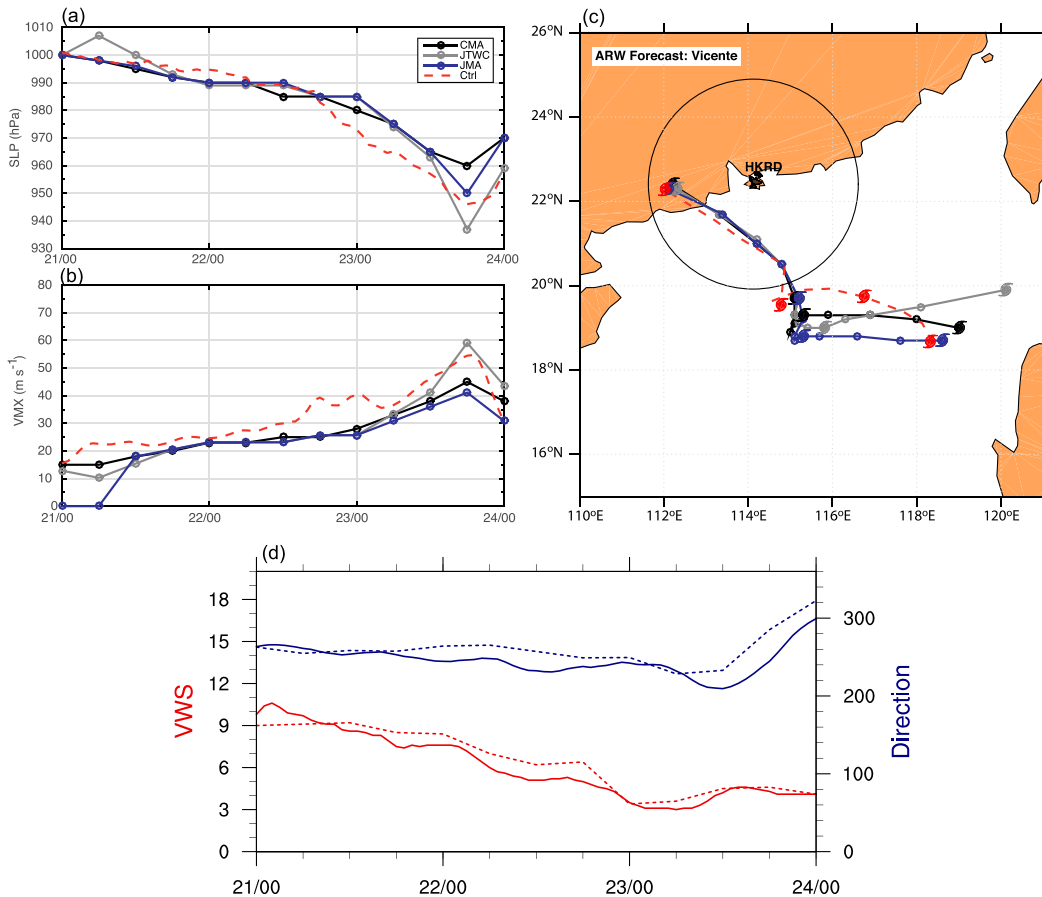


FIG. 4. Verification of simulated (a) minimum SLP (hPa), (b) 10-m maximum wind speed (m s^{-1}), and (c) track against best track datasets of CMA (black line), JTWC (gray line), and JMA (blue line). (d) Verification of the simulated magnitude (m s^{-1}) and direction ($^{\circ}$) of the large-scale 300–850-hPa VWS (solid) against that calculated from ERA-Interim data (dashed). The typhoon symbols in (c) denote the TC centers at 0000 UTC from 21 to 24 Jul.

(Fig. 4d). The 300–850-hPa VWS is calculated using the area-averaged azimuthal mean Cartesian wind components between 300- and 800-km radii from the TC center. The choice of both the vertical levels and the area average for environmental VWS is optimal for TCs over the SCS (Chen et al. 2015). The northeasterly VWS persisted during the whole integration period.

Since the RI phase of Vicente began over the central SCS where Doppler radar surveillance was unreachable (Fig. 1), the verification of the simulated storm structure evolution was primarily based on the comparison between modeled and satellite-observed infrared cloud-top brightness temperature (TBB). Nevertheless, the observational data obtained from Hkrd was employed to make a direct verification during the late RI phase after Vicente entered the northern SCS where it moved within the detectable range by Hkrd.

The overall evolution of the simulated storm structure was comparable to their observational counterpart based on TBB images. Prior to the RI (1200 UTC 22 July), deep

convection with colder cloud-top temperature developed preferentially on the downshear side (Figs. 5a,d). One day later, Vicente was in its RI phase and intensified to a typhoon with a clear eye and closed eyewall (Figs. 5b,e). The eyewall convection was dominated by a wavenumber-1 asymmetry with the strongest convective activity to the south of the TC center. Several spiral rainbands, originating from the northern eyewall and extending to the southeast and south, were distinct at this time. By 1800 UTC 23 July, just 2 h prior to landfall, the azimuthal coverage of deep convective clouds in the inner-core region was significantly increased and Vicente was close to its lifetime peak intensity as a super-typhoon (Figs. 5c,f).

The modeled TBB was somewhat warmer than the observed similar to the simulated Typhoon Megi in Wang and Wang (2014), suggesting that convection in the simulation could not penetrate as deep as those in the observation. In addition, the simulated spiral rainband in the southeast quadrant was farther away from

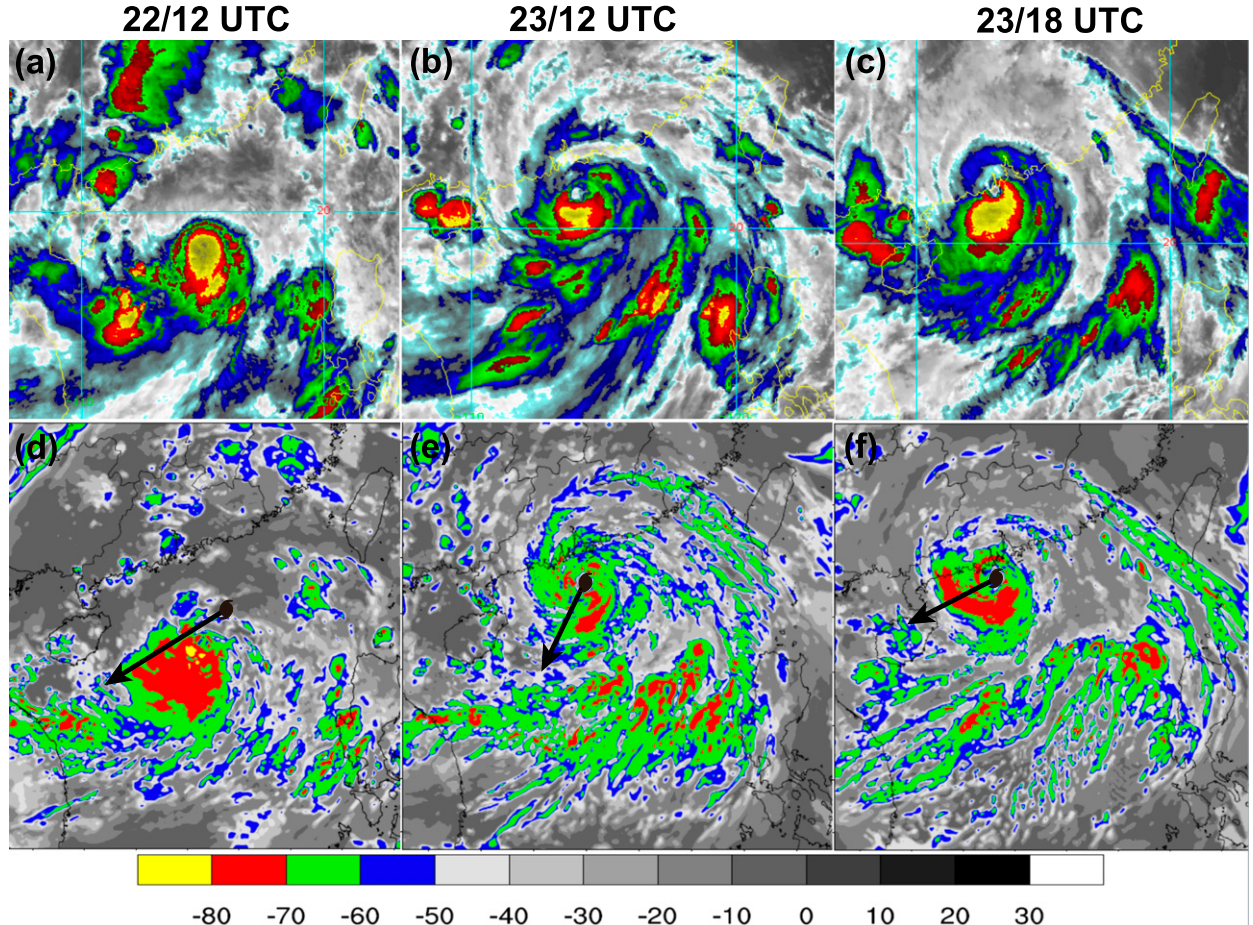


FIG. 5. Comparison of TBB ($^{\circ}$ C, shading) between the (top) satellite observations and (bottom) the WRF simulation for Typhoon Vicente at (a),(d) 1200 UTC 22 Jul; (b),(e) 1200 UTC 23 Jul; and (c),(f) 1800 UTC 23 Jul. The 300–850-hPa VWS (black arrow) are impinged on the model TBB in (d)–(f). The observed TBB data were obtained from http://rammb.cira.colostate.edu/products/tc_realtime/.

the storm core than that observed (e.g., Figs. 5b,e). Nevertheless, the model captured the overall inner-core structure and spiral rainbands in terms of convective activity.

Although the airborne Doppler radar observations have been used to verify high-resolution simulations of tropical cyclones (e.g., Chen and Gopalakrishnan 2015), the continuous inner-core structure evolution is hard to be captured by the airborne Doppler radar due to its coarse temporal resolution (\sim 30 min) and limited flight frequency. The ground-based Doppler radar with its fine temporal (\sim 6 min) and spatial ($1\text{ km} \times 1^{\circ}$) resolution was ideal for model verification. However, the verification of the numerically simulated TC against the ground-based Doppler radar observation has been rare, possibly due to the fact that ground-based Doppler radar observations for TCs were rarely available. Fortunately, most of the RI period of Vicente was in the Doppler coverage of the onshore HKRD. Based on the ground-based single Doppler radar retrieval technique—modified

ground-based velocity track display (MGBVTD)³—outlined in Chen et al. (2013), the primary circulation of Vicente could be accurately retrieved using the Doppler velocity data of HKRD. This provides a unique opportunity to make a direct comparison of the inner-core primary circulation between the modeled TC and the observed counterpart with fine temporal and spatial resolution for about 9 h.

In the following discussion, the MGBVTD retrievals were based on the 4-km GBVTD-simplex circulation center because the complete coverage of data at this height was available during the verification period. Figure 6

³The MGBVTD technique was developed to deduce the three-dimensional primary circulation of the landfalling TCs based on the ground-based single-Doppler radar datasets. It is able to retrieve the primary circulation accurately with the error of $\sim 2\text{ m s}^{-1}$ for the real TC cases [see Chen et al. (2013)].

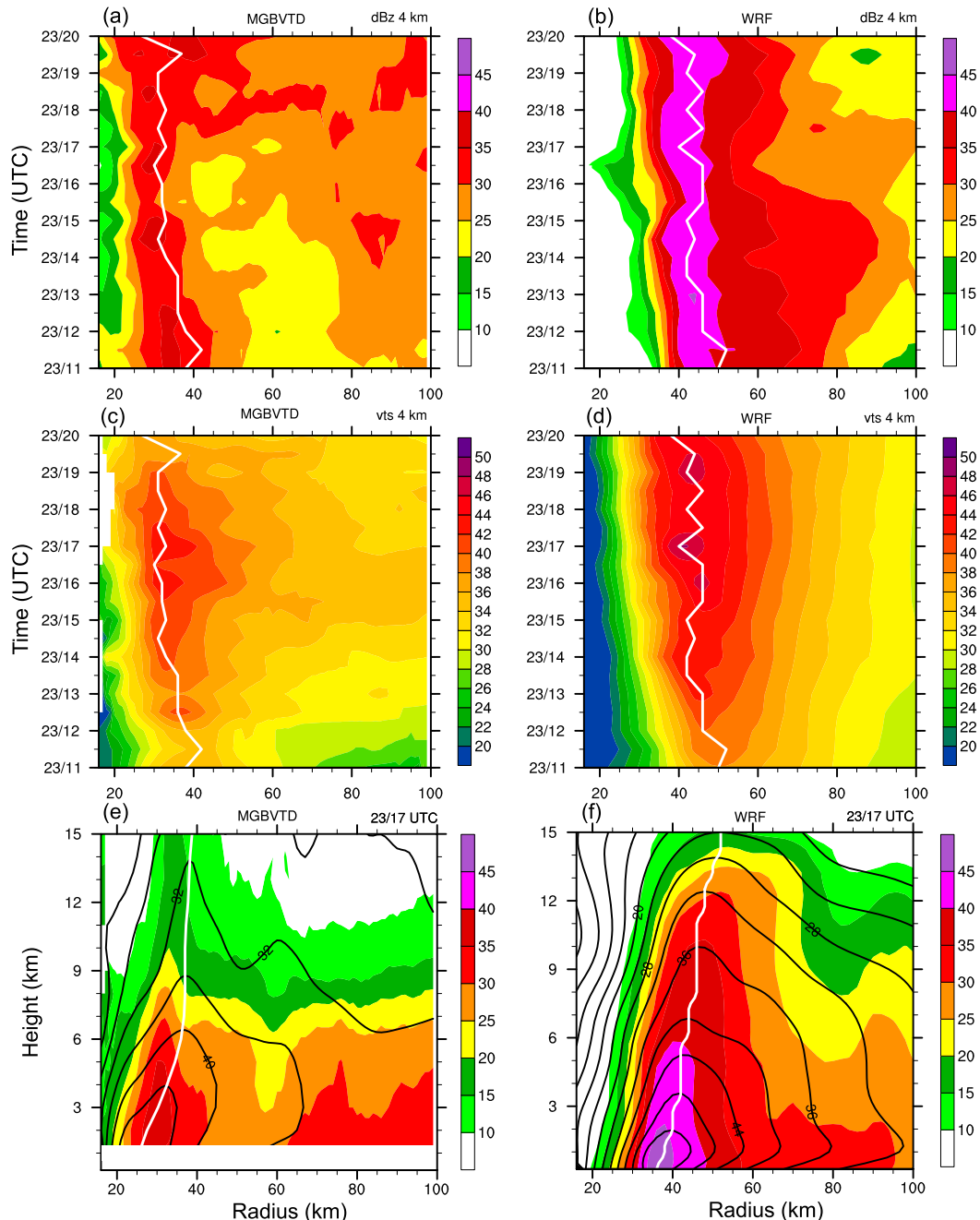


FIG. 6. (a)–(d) Time evolution of the (a),(c) MGBVTD-retrieved and (b),(d) WRF-simulated (a),(b) azimuthal mean radar reflectivity (dBZ) and (c),(d) tangential wind (m s^{-1}) at 4-km height from 0800 to 2030 UTC 23 Jul. (e),(f) The radius–height cross section of (e) the MGBVTD-retrieved and (f) the WRF-simulated axisymmetric radar reflectivity (dBZ, shading) and tangential wind (contoured at every 4 m s^{-1}) at 1700 UTC 23 Jul. White lines denote the radius of maximum wind (RMW).

shows the time evolution of the MGBVTD-retrieved (Figs. 6a,c,e) and the WRF-simulated (Figs. 6b,d,f) azimuthal mean radar reflectivity and the azimuthal mean tangential wind at the 4-km height from 0800 UTC 23 July to 2030 UTC 23 July, and also the corresponding

radius–height cross section of the MGBVTD-retrieved and the WRF-simulated azimuthal-mean tangential wind at 1700 UTC 23 July. The simulation successfully reproduced the eyewall contraction and significant enhancement of primary circulation during the late RI stage of

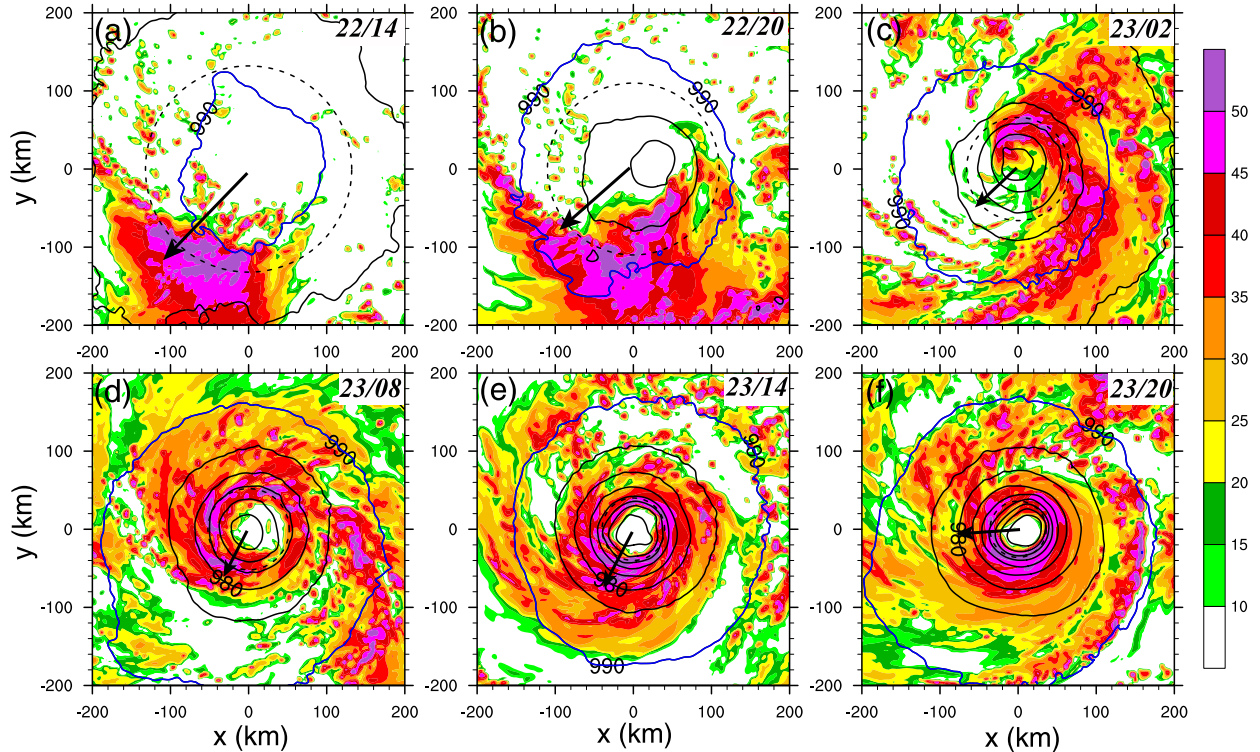


FIG. 7. (a)–(f) The 6-hourly WRF-simulated composite radar reflectivity (dBZ, shading) and sea level pressure (with contour interval of 5 hPa) from 1400 UTC 22 Jul to 2000 UTC 23 Jul. The 990-hPa isopleth is marked as a blue thick circle in each panel. The RMW at 2-km AGL is marked as the black dashed line in each panel. The black arrow denotes the 300–850-hPa large-scale VWS.

Vicente prior to its landfall as we can see from both the azimuthal mean radar reflectivity and tangential wind (Figs. 6a–d). The vertical structure of the azimuthal mean tangential wind was also reasonably simulated compared to the MGBVTD-retrieved counterpart despite a relatively small overestimation ($\sim 4 \text{ m s}^{-1}$) between 1.5- and 6-km heights in the simulation as shown for 1700 UTC 23 July (Figs. 6e,f). The eyewall both in the simulated and observed Vicente tilted outward with height with the maximum tangential wind decreasing with height, suggesting the elevated warm core of the storm at the mature stage (Figs. 6e,f). Note that the region with suppressed radar reflectivity outside the eyewall (near the 60-km radius in the MGBVTD retrievals and the 100-km radius in the WRF simulation) was the moat area.

Although the overall evolution of the simulated storm was quite similar to the observed, several discrepancies in the simulation could be identified in comparison with the radar observations as summarized below.

- 1) The simulated RMW at the 4-km height was approximately 10 km larger than the observed as it shrank from 50 to 35 km in the simulation (Figs. 6b,d) while the observed RMW contracted from 38 to ~ 27 km (Figs. 6a,c) during the verification period.
- 2) The radar reflectivity was overestimated by $\sim 5 \text{ dBZ}$ in the simulation as inferred from the time evolution of horizontal axisymmetric reflectivity (Figs. 6a,b) as well as the vertical cross section shown in Figs. 6e and 6f. The discrepancy could be explained by several reasons. First, the basic principle of radar reflectivity Z was retrieved based on the relationship with the mass of water content M (i.e., $Z = aM^b$). Previous observational studies have indicated that the combination of a, b depends on the properties of clouds (convective or stratiform), above or below the melting level in real TCs (Black 1990; Willis and Jorgensen 1981), whereas in the postprocessing model Z calculation, a and b were kept constant. Rogers et al. (2007) demonstrated that modification to the model Z calculation could significantly reduce the discrepancy between modeled and observed radar reflectivity. This could partially explain the higher radar reflectivity in the eyewall and moat region of the simulated Vicente (Fig. 6f).
- 3) The azimuthal mean tangential wind of the simulated Vicente was stronger ($\sim 5 \text{ m s}^{-1}$) than that retrieved from Doppler radar observations (Figs. 6e,f). It is important to keep in mind that the selection of the 4-km

height GBVTD-simplex center based on the MGBVTD technique would underestimate the retrieved primary circulation in the lower troposphere, in particular when the storm tilted in the vertical direction. Note that the supergradient nature of tangential wind within the boundary layer in the simulation could not be seen in the Doppler radar retrievals because the minimum reliable retrieval height was about 1.5 km due to Earth's curvature effects together with the altitude of radar site.

- 4) The tangential winds in the outer region expanded more rapidly in the MGBVTD-retrievals than that in the simulated counterpart ([Figs. 6c,d](#)), which was due to the active rainband activity therein ([Fig. 6a](#)).

Despite the existing discrepancies, the direct comparison between the MGBVTD retrievals and the model simulation indicated that overall the inner-core axisymmetric structure of the simulated Vicente was comparable to that observed. The comparison thus suggests that the model output can be used to examine the storm-scale evolution and physical processes contributing to the RI of Vicente.

4. Storm-scale evolution

Before the RI onset, the precipitation shield in Vicente exhibited a distinct wavenumber-1 structure with maximum precipitation downshear left at 1400 UTC 22 July ([Fig. 7a](#)), consistent with previous observational studies (Corbosiero and Molinari 2003; Chen et al. 2006; Molinari and Vollaro 2010a) and numerical simulations (Frank and Ritchie 1999, 2001; Rogers et al. 2003; Rappin and Nolan 2012). Later on, the precipitation shield began to spiral inward ([Figs. 7b,c](#)), which was accompanied by a central SLP deepening of about 15 hPa in 12 h. A complete eyewall formed by 0800 UTC 23 July ([Fig. 7d](#)) as the large-scale VWS dropped to its minimum value ([Fig. 4d](#)), indicating the stage of axisymmetric RI ([Figs. 7d–f](#)). The minimum central SLP dropped by another 20 hPa during this period.

The transition from the asymmetric to axisymmetric inner-core structure could be quantitatively measured by comparing the time evolutions of the azimuthal-mean symmetric kinetic energy (SKE) and the azimuthal-mean eddy kinetic energy (EKE)⁴ averaged within the lowest 5-km of the model atmosphere ([Figs. 8a,b](#)). The EKE maxima propagated toward the TC center from

1400 UTC 22 July to 0200 UTC 23 July. The feature that large EKE lasted several hours inside the innermost 30-km radii indicated significant asymmetric inner-core processes during this period will be detailed in Part II. By 0200 UTC 23 July after the eyewall formed, the EKE within the inner-core region almost disappeared, which was followed by a rapid enhancement of SKE near the RMW. Based on the distinct features before and after 0200 UTC 23 July, we defined two intensification stages, namely, the asymmetric intensification stage (the RI onset, 1200 UTC 22 July–0200 UTC 23 July) and the axisymmetric RI stage (0300 UTC 23 July–2000 UTC 23 July). The storm-scale evolution during the two stages is discussed below.

a. The RI onset

During the RI onset stage, the RMW shrank rapidly from 130 km at 1200 UTC 22 July to 60 km at 0200 UTC 23 July ([Fig. 8c](#)), consistent with the contraction of the SKE ([Fig. 8a](#)), while the maximum azimuthal-mean tangential wind at 2-km height increased slowly from 20 to 30 m s⁻¹ ([Fig. 8c](#)). The axisymmetric radar reflectivity around the RMW was less than 20 dBZ due to the incomplete coverage of the eyewall during this period ([Fig. 8c](#)). The boundary layer inflow well inside the RMW ([Figs. 8d](#)) was attributed to the weak inertial stability ($<0.5 \times 10^{-6} \text{ s}^{-2}$ just inside the RMW) when the inner-core structure was not well organized ([Figs. 7a–c](#)). It is worthwhile to note that the downshear convective activities near the RMW ([Fig. 8c](#)) were attributed to the balanced dynamics of the tilted TC vortex (not shown).

b. The axisymmetric RI stage

Benefited from the shrinking RMW and the gradual formation of a closed eyewall during the RI onset, the TC intensified efficiently in this stage. Both the radar reflectivity and the primary circulation at the 2-km height strengthened significantly. The former increased from 20 to 50 dBZ in the eyewall and the latter intensified from 30 to 50 m s⁻¹ ([Fig. 8c](#)). The eyewall contraction during this stage slowed down considerably compared with that during the RI onset stage. The RMW at the 2-km height contracted from 60 km at 0300 UTC to 35 km at 2000 UTC 23 July in the simulation ([Fig. 8](#)).

The azimuthal mean radial inflow near the RMW increased from 6 m s⁻¹ at the 0.25-km height during the RI onset stage to over 16 m s⁻¹ at the peak intensity of the storm at around 2000 UTC 23 July ([Fig. 8d](#)). As the storm intensified, the inertial stability near the RMW was almost tripled ([Fig. 8d](#)). The progressive radial inflow in response to eyewall heating and boundary layer friction rapidly decelerated and converged near the

⁴ EKE is defined as $(u'^2 + v'^2)/2$, where u' and v' are the asymmetric radial and tangential winds, respectively.

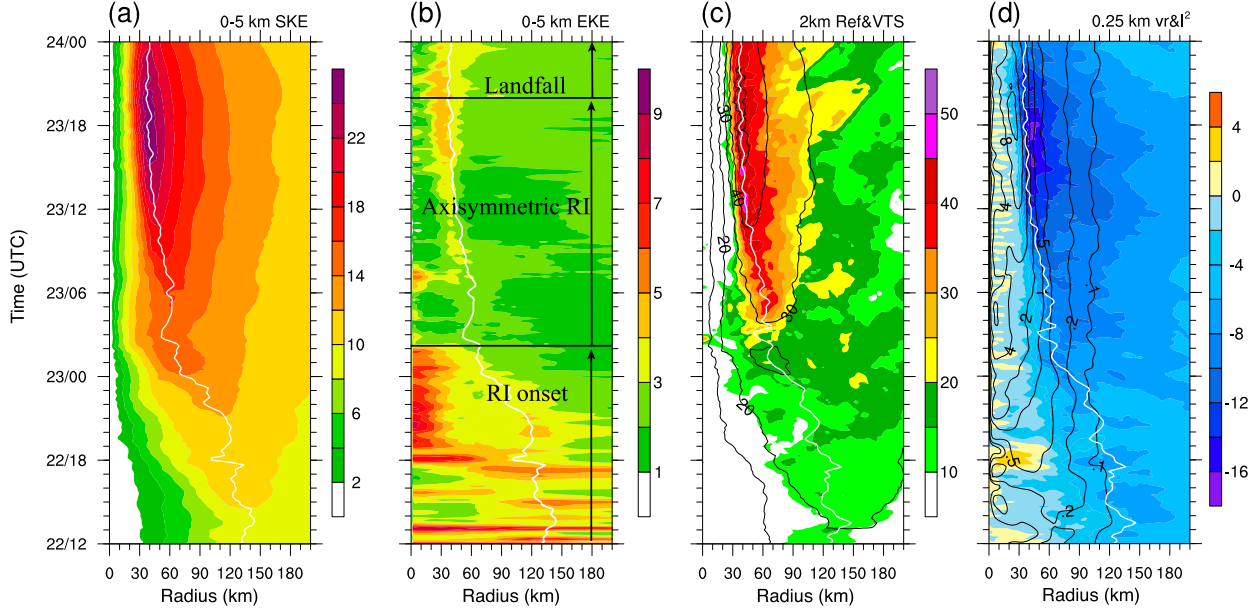


FIG. 8. Hovmöller diagrams of the azimuthally averaged (a) symmetric kinetic energy ($\text{m}^2 \text{s}^{-2}$, SKE), (b) eddy kinetic energy ($\text{m}^2 \text{s}^{-2}$, EKE) averaged between the surface and 5-km height, (c) radar reflectivity (dBZ, shading) and tangential wind (contoured at every 10 m s^{-1}) at 2-km height, and (d) radial inflow (m s^{-1} , shading) and inertial instability (contoured at $0.1, 0.2, 0.5, 1.0, 2.0, 4.0, 8.0, 12.0 \times 10^{-6} \text{ s}^{-2}$) at 0.25-km height. The inertial stability is defined as $I^2 = (f + \zeta)(f + 2v/r)$. The white lines in (a),(b) represent the averaged RMW in the 0–5-km layer, while in (c),(d) they represent the RMW at 2 km AGL.

RMW due to the strong inertial stability (Figs. 8c,d). This resulted in the strengthening of the radial mass and moisture convergence in the boundary layer, enhancing eyewall updrafts and thus diabatic heating in the eyewall and further intensifying the storm. In turn, the inertial stability near RMW was further enhanced and so was the heating efficiency. This formed a positive feedback for TC intensification, as discussed for the Typhoon Megi (2010) case in Wang and Wang (2014). However, the contraction rate of the RMW was decelerated also due to the strong inertial stability near RMW (Fig. 8d) that confined the strong inflow slightly outside the RMW at the mature stage. It is important to note that the contraction of the RMW ceased (~ 1400 UTC 23 July) long before the peak intensity was achieved (~ 1800 UTC 23 July), similar to the results in the idealized simulation (e.g., Stern et al. 2015) and the statistical analysis of real TCs (Qin et al. 2016).

5. Storm-scale tangential wind budget

To reveal the dynamical processes responsible for the spinup of the primary circulation of the simulated Vicente, the storm-relative azimuthal mean tangential wind budget was conducted in this section. In the cylindrical coordinate system centered at the mass centroid as mentioned in section 3a, the azimuthal mean tangential wind budget equation can be written as

$$\frac{\partial \bar{v}}{\partial t} = -\bar{u}(\bar{f} + \bar{\zeta}) - \frac{\bar{w}\partial \bar{v}}{\partial z} - \overline{u'\zeta'} - \frac{\bar{w}'\partial \bar{v}'}{\partial z} + \overline{\text{PBL}} + \overline{\text{DIFF}}. \quad (1)$$

The overbar in Eq. (1) denotes the azimuthal average and the prime denotes the deviation from the azimuthal average; u , v , and w denote storm-relative radial, tangential, and vertical winds, respectively; f and ζ are the Coriolis parameter and vertical component of relative vorticity, respectively; and PBL and DIFF are the tangential wind tendency due to vertical mixing (including surface friction) and horizontal diffusion, respectively. Four terms on the right-hand side are the mean radial flux of absolute mean vertical vorticity (MRAD), the vertical advection of the azimuthal mean tangential wind by the azimuthal mean vertical motion (MVAD), the radial eddy flux of perturbation vorticity (ERAD), and the vertical advection of asymmetric tangential wind by asymmetric vertical motion (EVAD). The budget was done for the two stages as discussed in section 4.

a. Budget A: The RI onset stage

During the RI onset stage, each term in Eq. (1) was integrated from 1600 UTC 22 July to 0200 UTC 23 July and the budget result was shown in Fig. 9. The integration period covered the period of rapid inward shift

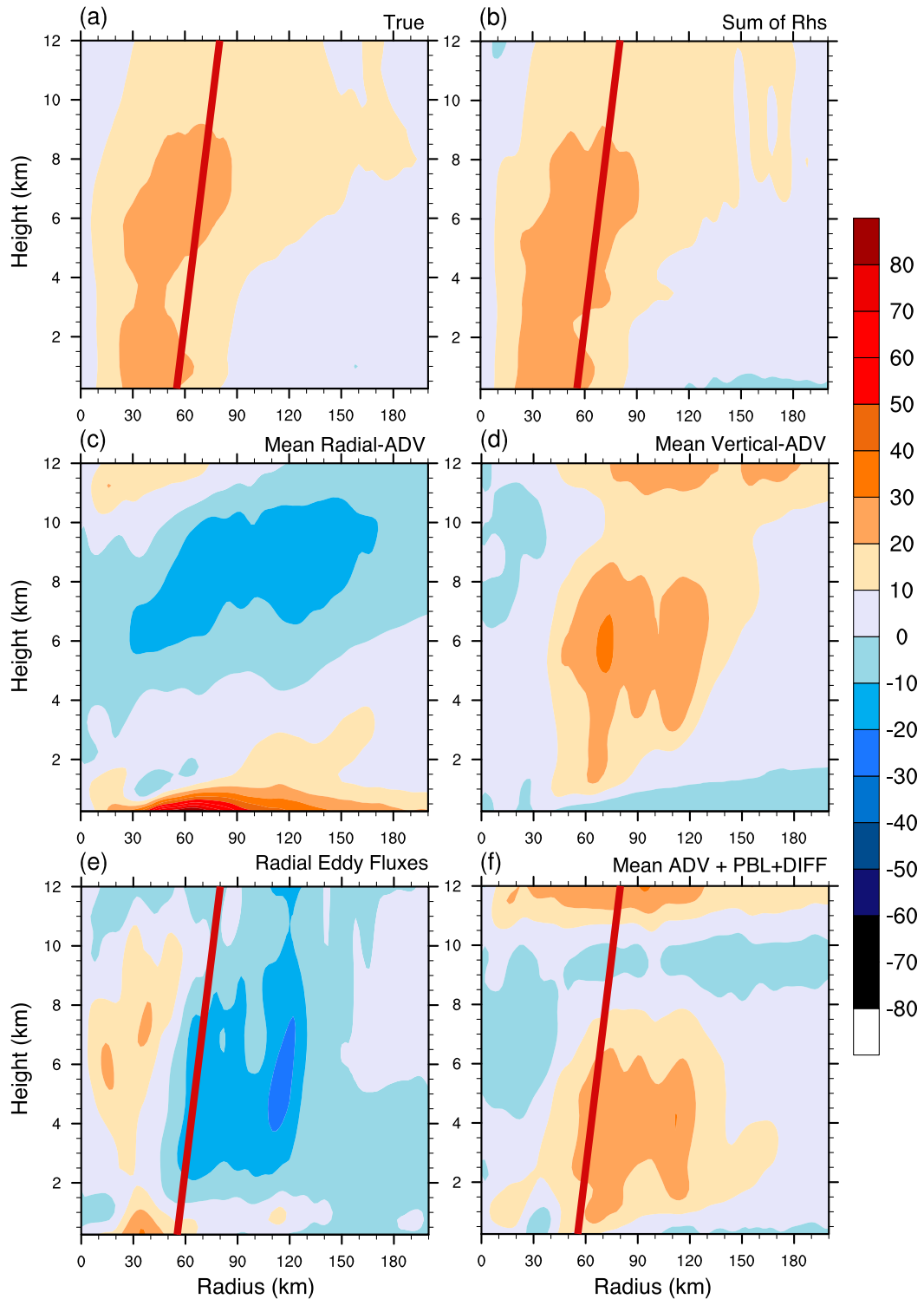


FIG. 9. Time-integrated azimuthal mean tangential wind tendency terms in Eq. (1) from 1600 UTC 22 Jul to 0200 UTC 23 Jul. The time integration of (a) true tangential wind tendency of the WRF simulation, (b) sum of all terms on the rhs of Eq. (1), (c) mean radial flux of absolute mean vertical vorticity (MRAD), (d) the vertical advection of the azimuthal mean tangential wind by the azimuthal mean vertical motion (MVAD), (e) the radial eddy flux of perturbation vorticity (ERAD), and (f) sum of mean advection terms (MRAD + MVAD) together with mean PBL and DIFF. The thick red line denotes the approximate RMW at the end of the integration period. The unit in each panel is m s^{-1} .

of large EKE (Fig. 8b) to reveal the key dynamical role of asymmetric eddies in the RI onset. Equation (1) was integrated forward with a time step of 10 min. The budget results (Figs. 9a,b) indicated that the true tangential wind tendency [lhs of Eq. (1)] during the RI onset was quite similar to the sum of the budget terms on the rhs of Eq. (1). The storm intensification during this period was mostly confined within the RMW (Figs. 9a,b) and was contributed mainly by eddy terms (Fig. 9e). In fact, the ERAD term was the dominant eddy term (Fig. 9e) whose effect was to accelerate (decelerate) the azimuthal mean primary circulation inside (outside) the RMW, contributing to the rapid contraction of the RMW. Hendricks et al. (2004) found a similar positive contribution by ERAD during the formation/intensification of TC Diana (1984) due to the significant inward flux of convectively induced vorticity anomalies (see their “budget B”).

The storm-scale spinup near and outside the RMW was contributed by the sum of mean tangential wind advection terms (Fig. 9f). The mean inflow in the boundary layer transported the absolute angular momentum inward, which was mostly offset by the surface friction effect (PBL term) as inferred from a comparison between Fig. 9c and Fig. 9f. The positive residual penetrated into the eyewall and was transported upward by the mean vertical motion within the eyewall (Figs. 9d,f). The insignificant spinup effect outside the RMW was ascribed to the counteracting effect between the mean advection and the eddy mixing terms (Figs. 9e,f).

b. Budget B: The axisymmetric RI stage

Different from the RI onset stage, the storm-scale spinup in the axisymmetric RI stage was concentrated in the eyewall region instead of inside of the RMW (Figs. 10a,b). The mean advection terms, MRAD and MVAD, were responsible for the storm intensification during this period. Similar to the intensification mechanism near the RMW in budget A, the positive residual mean tangential wind tendency (the sum of MRAD, PBL, and DIFF terms) within the boundary layer reached the eyewall region and extended upward throughout the troposphere by vertical advection in the eyewall (Figs. 10c,d,f). The strong negative MRAD just above the boundary layer (~ 2 -km height) reflected the existence of outflow associated with the local supergradient wind (Fig. 10c). Note that there were some discrepancies between the budgeted tangential wind tendency [the sum of the integrated tendencies on the rhs of Eq. (1)] and the true tendency calculated directly from the model outputs, in particular in the boundary layer (Figs. 10a,b). This was probably attributed to the sharp radial gradient of meteorological variables across the eyewall that could not be represented well using the local low-order differential scheme in the cylindrical coordinates. In

addition, the budget with the moving nest could also introduce some errors.

6. Environmental contribution to the RI onset

One of our main objectives in this study is to reveal the environmental contribution during the RI onset of Typhoon Vicente. In this section, the azimuthal mean tangential wind budget was repeated as done in budget A in section 5a but based on the reorganization of the budget in Eq. (1). Any variable A (wind or vorticity, etc.) was decomposed into an environmental component A_e ($L \geq 1500$ km) and a storm-scale component A_c ($L < 1500$ km), both including axisymmetric component and asymmetric component as shown in Eq. (2) below. The environmental component was obtained by employing a two-dimensional FFT spectral decomposition in the outmost domain. Then, we interpolated the filtered environmental component to the innermost domain and further separated the storm-scale component. Note that the storm-motion vector is subtracted from the environmental-scale winds as in Eq. (1). In this case the environmental component is projected onto the azimuthal mean and the asymmetric component relative to the moving storm center as well:

$$\begin{aligned} A &= A_e + A_c, \\ A_e &= \overline{A}_e + A'_e, \\ A_c &= \overline{A}_c + A'_c. \end{aligned} \quad (2)$$

The azimuthal mean tangential wind tendency on the lhs of Eq. (1) can be rewritten as

$$\frac{\partial \overline{v}}{\partial t} = \frac{\partial \overline{v}_e}{\partial t} + \frac{\partial \overline{v}_c}{\partial t}. \quad (3)$$

After taking the azimuthal mean of the rhs of Eq. (1), the budget equation can be rearranged to the following form:

$$\begin{aligned} \frac{\partial \overline{v}_c}{\partial t} &= \overline{\text{term1}} + \overline{\text{term2}} + \overline{\text{term3}} + \overline{\text{term4}} \\ &\quad + \overline{\text{PBL}} + \overline{\text{DIFF}} - \frac{\partial \overline{v}_e}{\partial t}, \end{aligned} \quad (4)$$

where $\overline{\text{term1}}$ to $\overline{\text{term4}}$ are analogous to the first four terms on the rhs in Eq. (1) and can be expressed as

$$\begin{aligned} \overline{\text{term1}} &= -\overline{u}_e(\overline{f} + \overline{\zeta}_e + \overline{\zeta}_c) - \overline{u}_c\overline{\zeta}_e - \overline{u}_c(\overline{f} + \overline{\zeta}_c), \\ \overline{\text{term2}} &= -\overline{w}_e \frac{\partial}{\partial z}(\overline{v}_c + \overline{v}_e) - \overline{w}_c \frac{\partial \overline{v}_e}{\partial z} - \overline{w}_c \frac{\partial \overline{v}_c}{\partial z}, \\ \overline{\text{term3}} &= -\overline{u}'_e(\overline{\zeta}'_e + \overline{\zeta}'_c) - \overline{u}'_c\overline{\zeta}'_e - \overline{u}'_c\overline{\zeta}'_c, \\ \overline{\text{term4}} &= -\overline{w}'_e \frac{\partial}{\partial z}(v'_e + v'_c) - \overline{w}_c \frac{\partial v'_e}{\partial z} - \overline{w}'_c \frac{\partial v'_c}{\partial z}. \end{aligned} \quad (5)$$

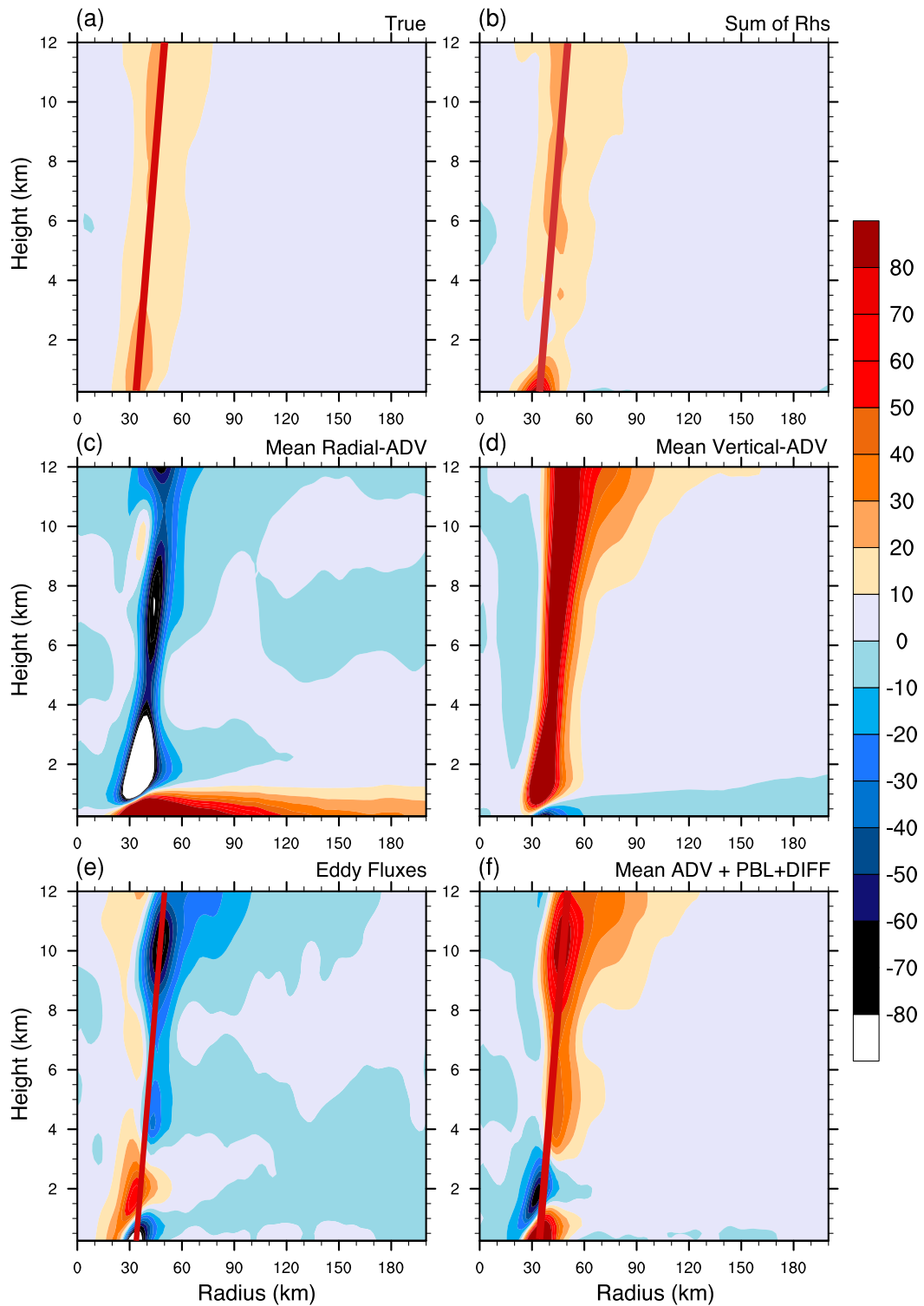


FIG. 10. (a)–(f) As in Fig. 9, but for the integration period from 0700 to 1800 UTC 23 Jul. In addition, the sum of radial eddy momentum flux and vertical advection of perturbation tangential wind ($\text{ERAD} + \text{EVAD}$) is shown in (e).

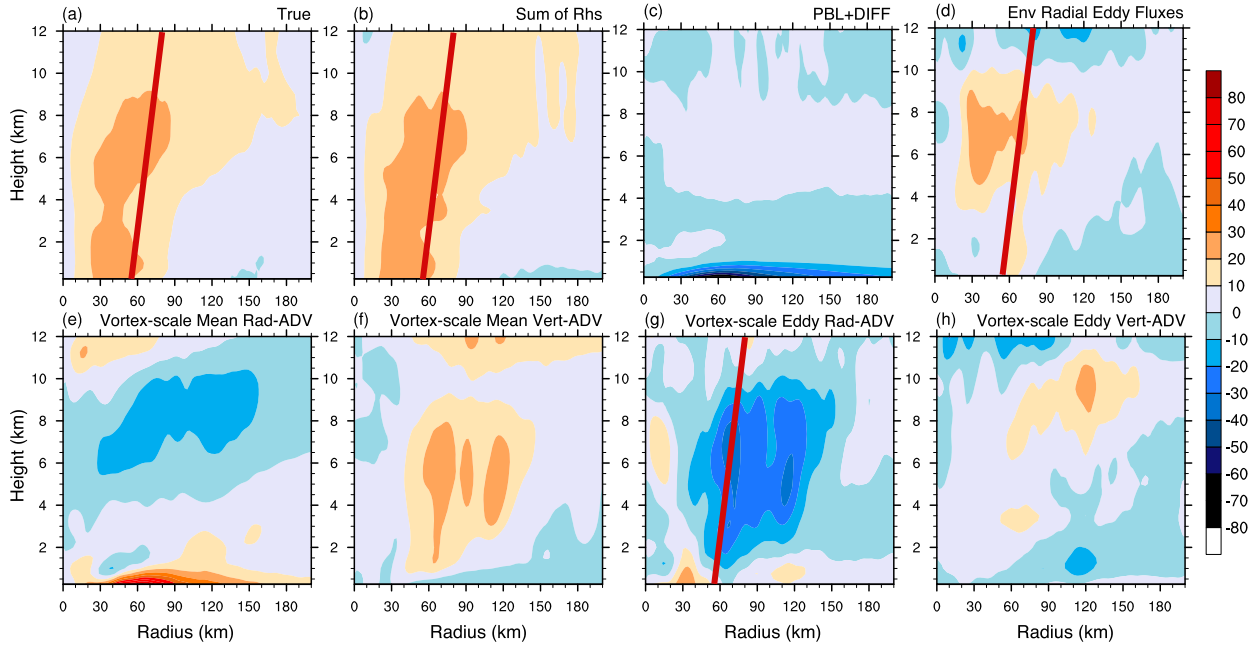


FIG. 11. (a)–(h) As in Fig. 9, but using the rearranged tangential wind budget in Eq. (4) based on scale separation. The time integration of (a) true tangential wind tendency of the WRF simulation, (b) the sum of all terms on the rhs of Eq. (4), (c) the sum of mean PBL and DIFF tendencies, (d) the environment–TC interaction term ($L \geq 1500$ km) (i.e., radial eddy flux) are shown. (e)–(h) The time integration of storm-scale ($L < 1500$ km) budget terms [see Eq. (5)]: (e) mean radial flux of absolute mean vertical vorticity, (f) the vertical advection of the azimuthal mean tangential wind by the azimuthal mean vertical motion, (g) the radial eddy flux of perturbation vorticity, and (h) the vertical advection of asymmetric tangential wind by asymmetric vertical motion.

The first two subterms in term₁ to term₄ are related to the interaction between the large-scale environment and the storm-scale vortex, while the third subterm involves the storm-scale processes only. Therefore, in the above budget equation, there are interactions among different scale motions, namely the large-scale environment, the storm-scale vortex, and the asymmetric components of the large-scale and the storm-scale motions. The integration period for the budget analysis below was the same as that in budget A in section 5a.

a. Monsoonal environmental flow

As discussed in section 5a, the spinup of the azimuthal mean circulation during the RI onset stage primarily resulted from the positive radial eddy momentum transport across the RMW. Given the fact that Vicente was embedded in the monsoon environment, it is expected that the monsoon trough might have contributed to the RI onset. Figure 11 shows various terms in the budget Eq. (4), which includes the major scale interaction processes. We found that the environment–TC interaction (i.e., the sum of the first two subterms in term₃) was responsible for the positive radial eddy momentum transport into the eye region, especially in the midtroposphere (Fig. 11d). The other environmental–TC interaction terms were unimportant in general (not

shown) since the environmental vertical velocity/vorticity projected onto the tangential component were at least one order smaller in magnitude than their storm-scale counterparts. The azimuthal mean tangential winds projected from the environmental flow [last term in Eq. (4)] were almost unchanged during the budget period (not shown) since the large-scale environmental flow often has a time scale of several days (Orlanski 1975).

To identify which process related to the environment–TC interaction was dominated in the RI onset, the first two subterms in term₃ were split into three subterms and the results were shown in Fig. 12. Since the magnitude of the environmental background vorticity was two orders smaller in magnitude than the storm-scale vorticity (Figs. 13a,c), it is not surprising that the interaction between the asymmetric radial winds projected from the environmental flow and the storm-scale vorticity anomalies was the dominant term to spin up the storm circulation (Fig. 12b). To understand the positive environmental contribution in the midtroposphere, Figs. 13a and 13b show the hourly composites of large-scale environmental wind and relative vorticity in the lower- and midtroposphere at 2200 UTC 22 July. Clearly, the two-dimensional FFT method successfully separated the background monsoon trough from the

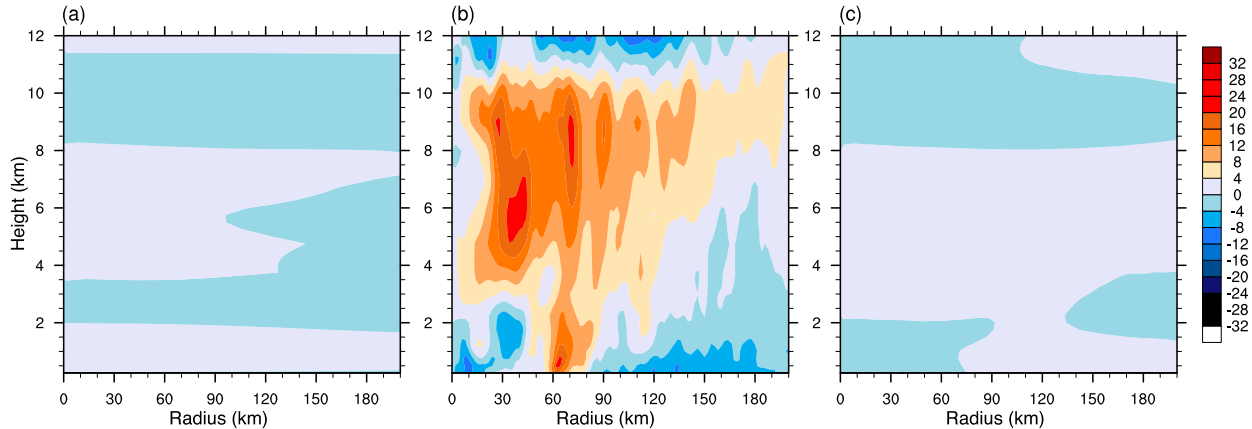


FIG. 12. Corresponding to Fig. 11d, the time integration of (a) $\overline{-u'_e \zeta'_e}$, (b) $\overline{-u'_e \zeta'_c}$, and (c) $\overline{-u'_e \zeta'_e}$ that split from the first two terms on the rhs of term³ in Eq. (5). The unit in each panel is $m s^{-1}$.

TC circulation. The monsoon flow prevailed over the TC circulation.

The asymmetric environmental winds and the storm-scale vorticity anomalies in the cylindrical coordinates were shown in Figs. 13c and 13d. The storm-scale vorticity anomalies were diffusively distributed in the boundary layer and the asymmetric radial winds projected from the monsoon flow advected both positive and negative storm-scale vorticity anomalies in and out inside the RMW (~ 90 km at this moment). Therefore, there was no distinct convergence of net positive radial eddy flux inside the RMW (Fig. 13e), which explained the absence of TC circulation enhancement in the lower troposphere contributed by the environment–TC interaction (Fig. 12b). On the contrary, the storm-scale vorticity anomalies in the midtroposphere were dominated by a wavenumber-1 structure with maximum vorticity anomalies to the left of the shear vector. In fact, the TC vortex was not vertically aligned under the forcing of moderate ambient VWS during the RI onset stage. Since the budget was performed for the axisymmetric TC vortex centered on the surface mass centroid, the tilted TC vortex would result in a wavenumber-1 structure. The asymmetric radial winds projected from the environmental flow advected net positive storm-scale vorticity anomalies inward from the downshear side and flushed out the negative storm-scale vorticity anomalies on the upshear side, resulting in the accumulation of net positive radial eddy momentum flux inside the RMW in the midtroposphere (Fig. 13f) and thus spinning up the primary circulation of the TC vortex during RI onset stage (Fig. 13d). This also suggests that the monsoon flow played a role in reducing the vertical tilt of the TC vortex. Note that the midlevel TC vortex, indicated approximately by the vorticity band to the left of the shear vector (Fig. 13d), had precessed

into the upshear flank at 2200 UTC 22 July. Given the fact that the strength of monsoon flow decreased with height (Figs. 13a,b), the northeasterly shear confined in the mid- to lower troposphere would reduce tilt of the TC vortex forced by the environmental VWS. More details of vertical alignment will be discussed in Part II.

The spinup of the primary circulation inside the RMW in the lower troposphere resulted mainly from the storm-scale radial eddy momentum flux (ERAD) as already shown in Fig. 11g. This indicates that the inner-core asymmetric processes played an important role in the RI onset, which will be further discussed in Part II.

b. Upper-level trough

During the RI onset stage, a branch of northeasterly winds (see black arrow in Fig. 14) in the front (west) of an inverted trough gradually shifted away from the TC circulation as the trough propagated westward at 200 hPa (Fig. 14). The poleward outflow emerged at around 2000 UTC 22 July (Fig. 14b) when the environmental VWS started to decrease significantly. At 0000 UTC 23 July, the poleward outflow matured and contributed to the formation of the equatorward outflow channel (Fig. 14c). Interestingly, the enhancement of the poleward outflow was concurrent with the cyclonic rotation of the downshear precipitation shield (Figs. 7b,c). We will show in Part II that this feature was ascribed to the downshear enhancement of convective activity and the associated vertical vortex alignment, which led to the shrinking of large-scale VWS. In contrast to the hypothesis by Shieh et al. (2013), we could not simply attribute the shrinking of VWS to the westward propagation of the upper-level inverted trough. Instead, we found that the storm-scale dynamical process was important to the enhancement of the poleward outflow and further to the setup of the equatorward

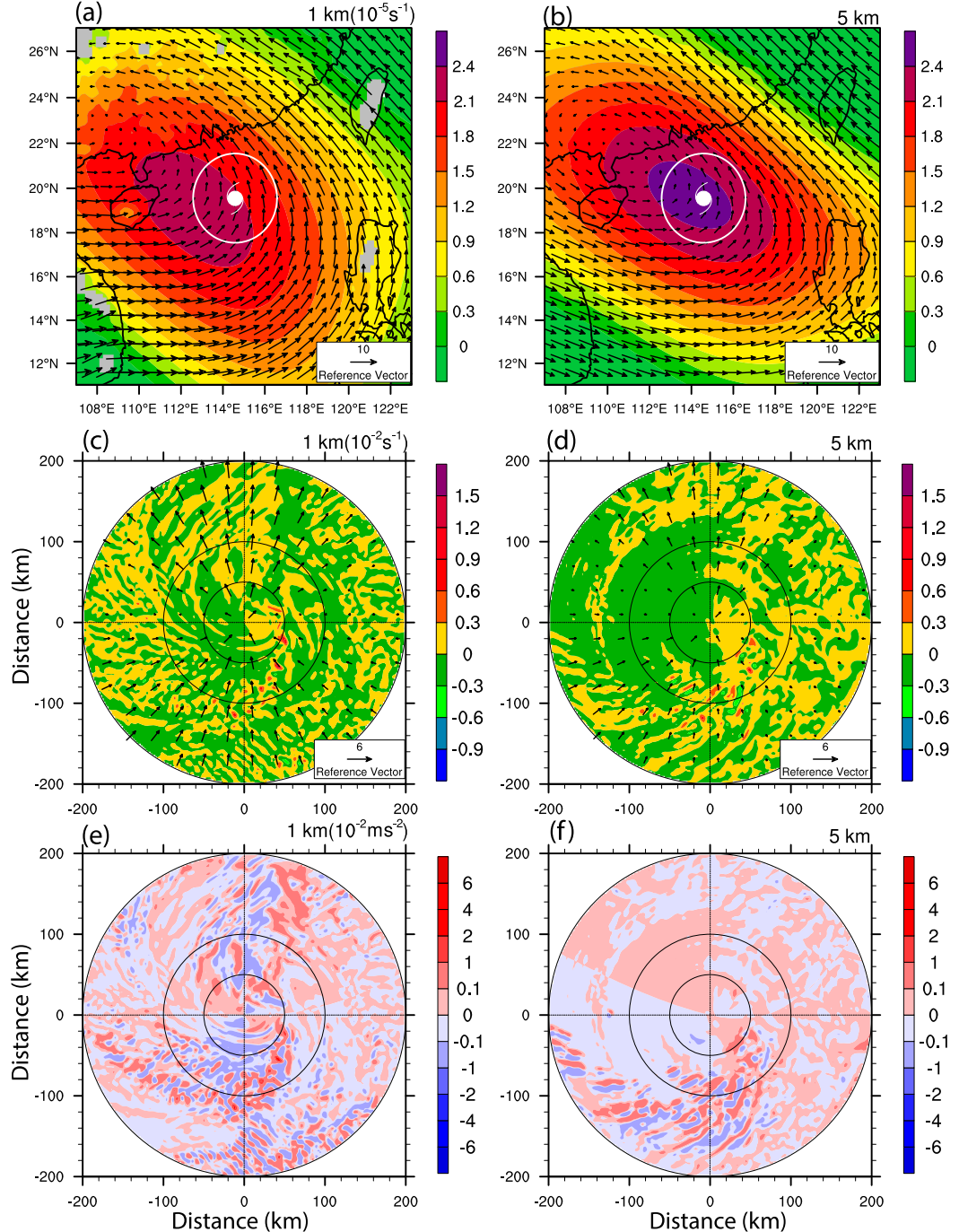


FIG. 13. Hourly composite of (a), (b) large-scale storm-relative environmental wind vectors ($m s^{-1}$) and vertical component of environmental relative vorticity ($10^{-5} s^{-1}$); (c), (d) asymmetric radial winds projected from the environmental flow ($m s^{-1}$) and storm-scale vorticity anomalies ($10^{-2} s^{-1}$); and (e), (f) $-u'_e \bar{v}'_e$ ($10^{-2} m s^{-2}$) at 2200 UTC 22 Jul. The left (right) column indicates the results at 1- (5)-km height. The white typhoon symbol in (a), (b) is the TC center and the white circle is the area shown in (c)–(f). The black circles in (c)–(f) indicate 50-, 100-, and 200-km radii, respectively.

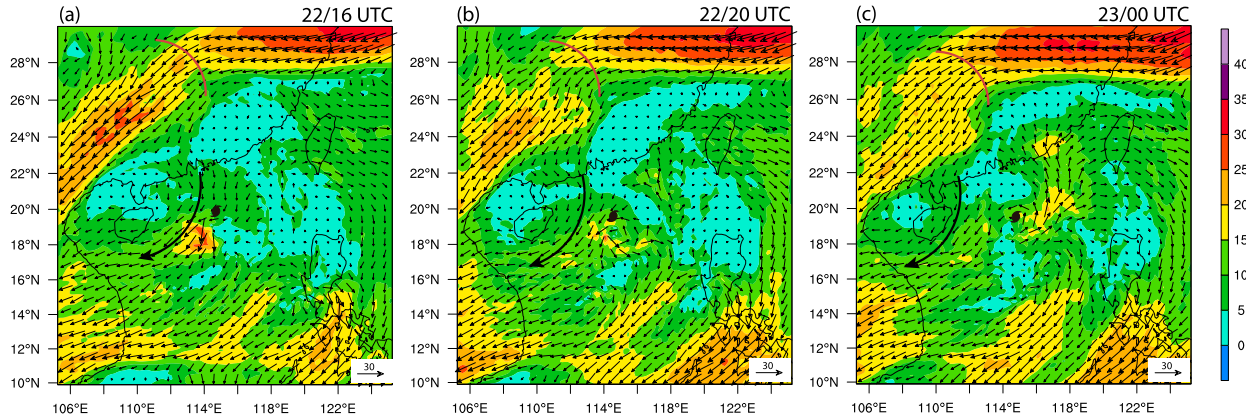


FIG. 14. The 200-hPa storm-relative wind vector and speed (m s^{-1} , shading) at (a) 1600 UTC 22 Jul, (b) 2000 UTC 22 Jul, and (c) 0000 UTC 23 Jul. The black typhoon symbol denotes the surface TC center. The red curve marks the trough line of the “inverted” trough. The black arrow denotes the northeasterly coming from the front of the “inverted” trough.

outflow channel, which contributed to the TC RI, as we will discuss in Part II.

7. Summary and conclusions

Typhoon Vicente (2012) intensified from a tropical storm to a supertyphoon within 18 h in the northern SCS before its landfall over south China. This extreme RI was missed in both regional and global model forecasts. In this study, a triply nested WRF simulation was performed to investigate the physical mechanisms responsible for the RI onset and the subsequent RI. The simulation was first verified against the best track and reanalysis data and also the multiplatform remote sensing observations, including the satellite TBB and ground-based Doppler radar retrievals. It was shown that the simulation reasonably reproduced the RI onset and the subsequent RI, sudden poleward track deflection. Also, the model generally captured the evolution of the inner- and outer-core structures despite of some discrepancies. The diagnostic analysis to understand the physical mechanisms responsible for the RI of Typhoon Vicente was conducted based on the simulation.

The analysis of the storm-scale evolution suggested two stages of the storm intensification: the asymmetric intensification related to the RI onset and the axisymmetric intensification related to the main RI stage. During the RI onset stage, the precipitation shield displayed a distinct wavenumber-1 asymmetry. The axisymmetric component exhibited a distinct contraction of the RMW with a relatively slow primary circulation spinup. The contraction of the RMW was ascribed to the radial eddy momentum transport as demonstrated by results from the storm-scale azimuthal-mean tangential wind budget. In contrast, the closed eyewall

formed shortly after the environmental VWS reduced to its minimum. This was followed by the axisymmetric RI stage during which the primary circulation intensified efficiently in response to the enhanced heating efficiency as the inertial stability amplified in the inner core.

We have shown that the interaction between the asymmetric radial winds projected from the monsoon flow and the storm-scale vorticity anomalies contributed predominantly to the spinup of the azimuthal mean tangential wind inside the RMW during RI onset stage, especially in the midtroposphere. The vorticity pattern in the midtroposphere exhibited a distinct VWS-induced wavenumber-1 asymmetric structure with positive vorticity anomalies to the left of shear vector and negative vorticity anomalies to the right, which was caused by the vortex tilt in the sheared environment. The prevailing monsoon flow in the midtroposphere advected the positive vorticity anomalies inward and negative vorticity anomalies outward across the storm core, resulting in the accumulation of net positive radial eddy momentum flux inside the RMW. This process considerably contributed to the spinup of the primary circulation in the midtroposphere. This also implies the positive role of the monsoon flow in the vertical alignment of an originally tilted vortex especially when the midlevel vortex precessed into the upshear flank. However, this process was insignificant in the lower troposphere where the storm-scale vorticity anomalies were diffusively distributed, showing no significant cyclonic eddy momentum convergence inside the RMW.

In the upper troposphere, the westward propagation of an “inverted” trough across the TC region was considered to play a role in the shrinking of the environmental VWS and thus contributed to the RI onset by Shieh et al. (2013). However, we found that the

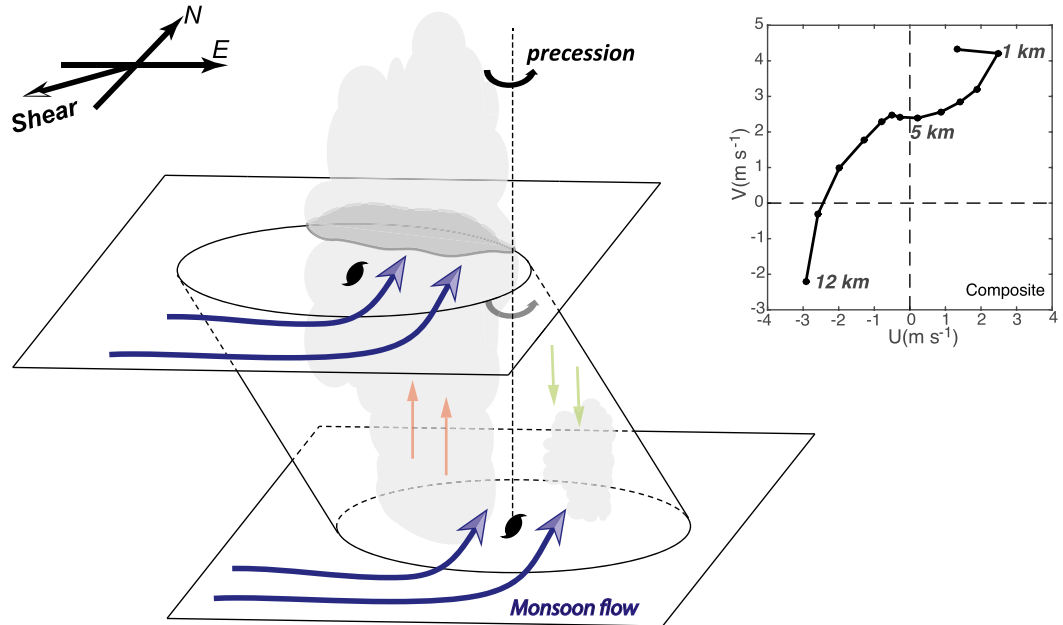


FIG. 15. Conceptual model of the interaction between monsoon trough and TC circulation contributing to the RI onset of Vicente. The blue arrow represents the monsoon flow. The dark gray shading denotes the midlevel positive vorticity anomalies in response to the shear-induced downshear ascent as well as convective activity (light gray plumes). The orange (green) arrows are the shear-induced mesoscale ascent (descent) in the upshear (downshear) flank of the eyewall. The inset in the top-right corner is the hodograph for the composite mean environmental winds averaged between 300- and 800-km radii from the storm center from the surface to 12-km height at a 1-km interval. The composite time period was the same as the integration period in Fig. 9.

reduction of the large-scale VWS was partially related to the inner-core processes, including the strong downshear convective activity and the vertical alignment of the storm-scale circulation. We will show in Part II that the divergent outflow in the upper troposphere was mainly a response to the downshear convective rainband, which began to rotate cyclonically before the rapid shrinking of the large-scale VWS, suggesting that the storm-scale and inner-core-scale processes may modify the large-scale VWS, in particular over the storm core region.

The RI of weak TCs embedded in moderate large-scale VWS is often connected to the spiral entrainment of downshear convection into the storm core region (Sitkowski and Barnes 2009; Shelton and Molinari 2009). The commensurate amount of convectively diabatic heating in the inner-core region with high inertial stability can effectively spin up the cyclonic circulation as inferred from the balanced vortex dynamics (Schubert and Hack 1982; Nolan et al. 2007; Vigh and Schubert 2009). Moreover, the so-called downshear reformation of a sheared TC was analyzed in some details by Molinari et al. (2004, 2006). They showed that the downshear convectively induced strong vorticity core interacted with the weak TC circulation and was

eventually wrapped into the TC center, leading to the high vorticity core and RI of the storm.

We will show in Part II that the large-scale VWS triggering RI onset is more complicated than the overall picture documented in previous studies. The inner-core dynamics, including the vertical alignment of the sheared-induced tilted vortex and the associated convective activity, needs to be examined in details for a complete understanding. Nevertheless, from the large-scale and the storm-scale viewpoint for the Typhoon Vicente case, as summarized in Fig. 15, the moist monsoon flow extending from the lower to midtroposphere, counteraligned with the shear direction, alleviated the dry air intrusion of upshear descent, and encouraged the downshear lifting and convective activities, hence, suppressing the negative effect of the environmental VWS. In this way, we proposed an adaptive RI mechanism involving the positive feedback between the monsoon trough and the embedded TC circulation. On one hand, the monsoon trough contributed to the downshear momentum flux into the storm core, resulting in the vertical vortex alignment against the environmental VWS. On the other hand, convective clusters generated in the monsoon flow formed a spiral rainband, once the rainband was wrapped into the inner core of the storm, both

diabatic heating and the associated vorticity anomalies would spin up the primary circulation of the storm. The details involving the inner-core dynamics and convective processes are referred to Part II.

Acknowledgments. The authors thank three anonymous reviewers for their constructive comments on the original manuscript. This study has been supported by the National Basic Research and Development Project (973 program) of China under Contract 2015CB452805, the National Natural Science Foundation of China under Grants 41322032, 41605033, 41275031, 41130964, and 41375068, and in part by NSF Grant AGS-1326524. We thank Dr. Chunxi Zhang of IPRC for his help with the model setup. We also appreciate Hong Kong Observatory for providing us the ground-based Doppler radar datasets used in our model verification.

REFERENCES

- Black, R. A., 1990: Radar reflectivity–ice water content relationships for use above the melting level in hurricanes. *J. Appl. Meteor.*, **29**, 955–961, doi:[10.1175/1520-0450\(1990\)029<955:RRIWCR>2.0.CO;2](https://doi.org/10.1175/1520-0450(1990)029<955:RRIWCR>2.0.CO;2).
- Chen, H., and D.-L. Zhang, 2013: On the rapid intensification of Hurricane Wilma (2005). Part II: Convective bursts and the upper-level warm core. *J. Atmos. Sci.*, **70**, 146–162, doi:[10.1175/JAS-D-12-062.1](https://doi.org/10.1175/JAS-D-12-062.1).
- , and S. G. Gopalakrishnan, 2015: A study on the asymmetric rapid intensification of Hurricane Earl (2010) using the HWRF system. *J. Atmos. Sci.*, **72**, 531–550, doi:[10.1175/JAS-D-14-0097.1](https://doi.org/10.1175/JAS-D-14-0097.1).
- Chen, S. S., J. A. Knaff, and F. D. Marks, 2006: Effects of vertical wind shear and storm motion on tropical cyclone rainfall asymmetries deduced from TRMM. *Mon. Wea. Rev.*, **134**, 3190–3208, doi:[10.1175/MWR3245.1](https://doi.org/10.1175/MWR3245.1).
- Chen, X., K. Zhao, W.-C. Lee, B. Jong-Dao Jou, M. Xue, and P. R. Harasti, 2013: The improvement to the environmental wind and tropical cyclone circulation retrievals with the modified GBVTD (MGBVTD) technique. *J. Appl. Meteor. Climatol.*, **52**, 2493–2508, doi:[10.1175/JAMC-D-13-031.1](https://doi.org/10.1175/JAMC-D-13-031.1).
- , Y. Wang, and K. Zhao, 2015: Synoptic flow patterns and large-scale characteristics associated with rapidly intensifying tropical cyclones in the South China Sea. *Mon. Wea. Rev.*, **143**, 64–87, doi:[10.1175/MWR-D-13-00338.1](https://doi.org/10.1175/MWR-D-13-00338.1).
- China Meteorological Administration (CMA), 2012: *Yearbook of Tropical Cyclone* (in Chinese). China Meteorological Press, 239 pp.
- Corbosiero, K. L., and J. Molinari, 2003: The relationship between storm motion, vertical wind shear, and convective asymmetries in tropical cyclones. *J. Atmos. Sci.*, **60**, 366–376, doi:[10.1175/1520-0469\(2003\)060<0366:TRBSMV>2.0.CO;2](https://doi.org/10.1175/1520-0469(2003)060<0366:TRBSMV>2.0.CO;2).
- DeMaria, M., J.-J. Baik, and J. Kaplan, 1993: Upper level angular momentum fluxes and tropical cyclone intensity change. *J. Atmos. Sci.*, **50**, 1133–1147, doi:[10.1175/1520-0469\(1993\)050<1133:ULEAMF>2.0.CO;2](https://doi.org/10.1175/1520-0469(1993)050<1133:ULEAMF>2.0.CO;2).
- , C. R. Sampson, J. A. Knaff, and K. D. Musgrave, 2014: Is tropical cyclone intensity guidance improving? *Bull. Amer. Meteor. Soc.*, **95**, 387–398, doi:[10.1175/BAMS-D-12-00240.1](https://doi.org/10.1175/BAMS-D-12-00240.1).
- Dudhia, J., 1989: Numerical study of convection observed during the Winter Monsoon Experiment using a mesoscale two-dimensional model. *J. Atmos. Sci.*, **46**, 3077–3107, doi:[10.1175/1520-0469\(1989\)046<3077:NSOCOD>2.0.CO;2](https://doi.org/10.1175/1520-0469(1989)046<3077:NSOCOD>2.0.CO;2).
- Elsberry, R. L., T. D. B. Lambert, and M. A. Boothe, 2007: Accuracy of Atlantic and eastern North Pacific tropical cyclone intensity forecast guidance. *Wea. Forecasting*, **22**, 747–762, doi:[10.1175/WAF1015.1](https://doi.org/10.1175/WAF1015.1).
- Enagonio, J., and M. T. Montgomery, 2001: Tropical cyclogenesis via convectively forced vortex Rossby waves in a shallow water primitive equation model. *J. Atmos. Sci.*, **58**, 685–706, doi:[10.1175/1520-0469\(2001\)058<0685:TCVCFV>2.0.CO;2](https://doi.org/10.1175/1520-0469(2001)058<0685:TCVCFV>2.0.CO;2).
- Fang, J., and F. Zhang, 2010: Initial development and genesis of Hurricane Dolly (2008). *J. Atmos. Sci.*, **67**, 655–672, doi:[10.1175/2009JAS3115.1](https://doi.org/10.1175/2009JAS3115.1).
- Frank, W. M., and E. A. Ritchie, 1999: Effects of environmental flow upon tropical cyclone structure. *Mon. Wea. Rev.*, **127**, 2044–2061, doi:[10.1175/1520-0493\(1999\)127<2044:EOEFUT>2.0.CO;2](https://doi.org/10.1175/1520-0493(1999)127<2044:EOEFUT>2.0.CO;2).
- , and —, 2001: Effects of vertical wind shear on the intensity and structure of numerically simulated hurricanes. *Mon. Wea. Rev.*, **129**, 2249–2269, doi:[10.1175/1520-0493\(2001\)129<2249:EOVWSO>2.0.CO;2](https://doi.org/10.1175/1520-0493(2001)129<2249:EOVWSO>2.0.CO;2).
- Gray, W. M., 1968: Global view of the origin of tropical disturbances and storms. *Mon. Wea. Rev.*, **96**, 669–700, doi:[10.1175/1520-0493\(1968\)096<0669:GVOTOO>2.0.CO;2](https://doi.org/10.1175/1520-0493(1968)096<0669:GVOTOO>2.0.CO;2).
- Hendricks, E. A., M. T. Montgomery, and C. A. Davis, 2004: The role of “vortical” hot towers in the formation of Tropical Cyclone Diana (1984). *J. Atmos. Sci.*, **61**, 1209–1232, doi:[10.1175/1520-0469\(2004\)061<1209:TROVHT>2.0.CO;2](https://doi.org/10.1175/1520-0469(2004)061<1209:TROVHT>2.0.CO;2).
- Heymsfield, G. M., J. Simpson, J. Halverson, L. Tian, E. Ritchie, and J. Molinari, 2006: Structure of highly sheared Tropical Storm Chantal during CAMEX-4. *J. Atmos. Sci.*, **63**, 268–287, doi:[10.1175/JAS3602.1](https://doi.org/10.1175/JAS3602.1).
- Holland, G. J., 1995: Scale interaction in the western Pacific monsoon. *Meteor. Atmos. Phys.*, **56**, 57–79, doi:[10.1007/BF01022521](https://doi.org/10.1007/BF01022521).
- Jones, S. C., 1995: The evolution of vortices in vertical shear. I: Initially barotropic vortices. *Quart. J. Roy. Meteor. Soc.*, **121**, 821–851, doi:[10.1002/qj.49712152406](https://doi.org/10.1002/qj.49712152406).
- Kain, J. S., and J. M. Fritsch, 1993: Convective parameterization for mesoscale models: The Kain–Fritsch scheme. *The Representation of Cumulus Convection in Numerical Models*, K. A. Emanuel and D. J. Raymond, Eds., Amer. Meteor. Soc., 165–170.
- Kaplan, J., and M. DeMaria, 2003: Large-scale characteristics of rapidly intensifying tropical cyclones in the North Atlantic basin. *Wea. Forecasting*, **18**, 1093–1108, doi:[10.1175/1520-0434\(2003\)018<1093:LCORIT>2.0.CO;2](https://doi.org/10.1175/1520-0434(2003)018<1093:LCORIT>2.0.CO;2).
- , —, and J. A. Knaff, 2010: A revised tropical cyclone rapid intensification index for the Atlantic and eastern North Pacific basins. *Wea. Forecasting*, **25**, 220–241, doi:[10.1175/2009WAF2222280.1](https://doi.org/10.1175/2009WAF2222280.1).
- Lee, W.-C., and F. D. Marks, 2000: Tropical cyclone kinematic structure retrieved from single-Doppler radar observations. Part II: The GBVTD-simplex center finding algorithm. *Mon. Wea. Rev.*, **128**, 1925–1936, doi:[10.1175/1520-0493\(2000\)128<1925:TCKSRF>2.0.CO;2](https://doi.org/10.1175/1520-0493(2000)128<1925:TCKSRF>2.0.CO;2).
- Li, X., R. He, Z. Duan, and N. Wu, 2014: Analysis on the unusual track and intensification of Typhoon “Vicente.” *J. Trop. Meteor.*, **30**, 533–541.
- Mlawer, E. J., S. J. Taubman, P. D. Brown, M. J. Iacono, and S. A. Clough, 1997: Radiative transfer for inhomogeneous atmospheres: RRTM, a validated correlated-k model for the

- longwave. *J. Geophys. Res.*, **102**, 16 663–16 682, doi:[10.1029/97JD00237](https://doi.org/10.1029/97JD00237).
- Molinari, J., and D. Vollaro, 2010a: Distribution of helicity, CAPE, and shear in tropical cyclones. *J. Atmos. Sci.*, **67**, 274–284, doi:[10.1175/2009JAS3090.1](https://doi.org/10.1175/2009JAS3090.1).
- , and —, 2010b: Rapid intensification of a sheared tropical storm. *Mon. Wea. Rev.*, **138**, 3869–3885, doi:[10.1175/2010MWR3378.1](https://doi.org/10.1175/2010MWR3378.1).
- , and —, 2013: What percentage of western North Pacific tropical cyclones form within the monsoon trough? *Mon. Wea. Rev.*, **141**, 499–505, doi:[10.1175/MWR-D-12-00165.1](https://doi.org/10.1175/MWR-D-12-00165.1).
- , —, and K. L. Corbosiero, 2004: Tropical cyclone formation in a sheared environment: A case study. *J. Atmos. Sci.*, **61**, 2493–2509, doi:[10.1175/JAS3291.1](https://doi.org/10.1175/JAS3291.1).
- , P. Dodge, D. Vollaro, K. L. Corbosiero, and F. Marks, 2006: Mesoscale aspects of the downshear reformation of a tropical cyclone. *J. Atmos. Sci.*, **63**, 341–354, doi:[10.1175/JAS3591.1](https://doi.org/10.1175/JAS3591.1).
- Möller, J. D., and M. T. Montgomery, 2000: Tropical cyclone evolution via potential vorticity anomalies in a three-dimensional balance model. *J. Atmos. Sci.*, **57**, 3366–3387, doi:[10.1175/1520-0469\(2000\)057<3366:TCEVPV>2.0.CO;2](https://doi.org/10.1175/1520-0469(2000)057<3366:TCEVPV>2.0.CO;2).
- Montgomery, M. T., and R. J. Kallenbach, 1997: A theory for vortex Rossby-waves and its application to spiral bands and intensity changes in hurricanes. *Quart. J. Roy. Meteor. Soc.*, **123**, 435–465, doi:[10.1002/qj.49712353810](https://doi.org/10.1002/qj.49712353810).
- , M. E. Nicholls, T. A. Cram, and A. B. Saunders, 2006: A vortical hot tower route to tropical cyclogenesis. *J. Atmos. Sci.*, **63**, 355–386, doi:[10.1175/JAS3604.1](https://doi.org/10.1175/JAS3604.1).
- Nguyen, L. T., and J. Molinari, 2012: Rapid intensification of a sheared, fast-moving hurricane over the Gulf Stream. *Mon. Wea. Rev.*, **140**, 3361–3378, doi:[10.1175/MWR-D-11-00293.1](https://doi.org/10.1175/MWR-D-11-00293.1).
- , and —, 2015: Simulation of the downshear reformation of a tropical cyclone. *J. Atmos. Sci.*, **72**, 4529–4551, doi:[10.1175/JAS-D-15-0036.1](https://doi.org/10.1175/JAS-D-15-0036.1).
- , —, and D. Thomas, 2014: Evaluation of tropical cyclone center identification methods in numerical models. *Mon. Wea. Rev.*, **142**, 4326–4339, doi:[10.1175/MWR-D-14-0044.1](https://doi.org/10.1175/MWR-D-14-0044.1).
- Noh, Y., W. G. Cheon, S. Y. Hong, and S. Raasch, 2003: Improvement of the k-profile model for the planetary boundary layer based on large eddy simulation data. *Bound.-Layer Meteor.*, **107**, 401–427, doi:[10.1023/A:1022146015946](https://doi.org/10.1023/A:1022146015946).
- Nolan, D. S., Y. Moon, and D. P. Stern, 2007: Tropical cyclone intensification from asymmetric convection: Energetics and efficiency. *J. Atmos. Sci.*, **64**, 3377–3405, doi:[10.1175/JAS3988.1](https://doi.org/10.1175/JAS3988.1).
- Orlanski, I., 1975: A rational subdivision of scales for atmospheric processes. *Bull. Amer. Meteor. Soc.*, **56** (5), 527–530.
- Pendergrass, A. G., and H. E. Willoughby, 2009: Diabatically induced secondary flows in tropical cyclones. Part I: Quasi-steady forcing. *Mon. Wea. Rev.*, **137**, 805–821, doi:[10.1175/2008MWR2657.1](https://doi.org/10.1175/2008MWR2657.1).
- Qin, N., D.-L. Zhang, and Y. Li, 2016: A statistical analysis of steady eyewall sizes associated with rapidly intensifying hurricanes. *Wea. Forecasting*, **31**, 737–742, doi:[10.1175/WAF-D-16-0016.1](https://doi.org/10.1175/WAF-D-16-0016.1).
- Rappin, E. D., and D. S. Nolan, 2012: The effect of vertical shear orientation on tropical cyclogenesis. *Quart. J. Roy. Meteor. Soc.*, **138**, 1035–1054, doi:[10.1002/qj.977](https://doi.org/10.1002/qj.977).
- Reasor, P. D., M. T. Montgomery, and L. D. Grasso, 2004: A new look at the problem of tropical cyclones in vertical shear flow: Vortex resiliency. *J. Atmos. Sci.*, **61**, 3–22, doi:[10.1175/1520-0469\(2004\)061<0003:ANLATP>2.0.CO;2](https://doi.org/10.1175/1520-0469(2004)061<0003:ANLATP>2.0.CO;2).
- , M. D. Eastin, and J. F. Gamache, 2009: Rapidly intensifying Hurricane Guillermo (1997). Part I: Low-wavenumber structure and evolution. *Mon. Wea. Rev.*, **137**, 603–631, doi:[10.1175/2008MWR2487.1](https://doi.org/10.1175/2008MWR2487.1).
- Riemer, M., M. T. Montgomery, and M. E. Nicholls, 2010: A new paradigm for intensity modification of tropical cyclones: Thermodynamic impact of vertical wind shear on the inflow layer. *Atmos. Chem. Phys.*, **10**, 3163–3188, doi:[10.5194/acp-10-3163-2010](https://doi.org/10.5194/acp-10-3163-2010).
- Ritchie, E. A., and G. J. Holland, 1997: Scale interactions during the formation of Typhoon Irving. *Mon. Wea. Rev.*, **125**, 1377–1396, doi:[10.1175/1520-0493\(1997\)125<1377:SIDTFO>2.0.CO;2](https://doi.org/10.1175/1520-0493(1997)125<1377:SIDTFO>2.0.CO;2).
- , and —, 1999: Large-scale patterns associated with tropical cyclogenesis in the western Pacific. *Mon. Wea. Rev.*, **127**, 2027–2043, doi:[10.1175/1520-0493\(1999\)127<2027:LPAWT>2.0.CO;2](https://doi.org/10.1175/1520-0493(1999)127<2027:LPAWT>2.0.CO;2).
- Rogers, R., S. Chen, J. Tenerelli, and H. Willoughby, 2003: A numerical study of the impact of vertical shear on the distribution of rainfall in Hurricane Bonnie (1998). *Mon. Wea. Rev.*, **131**, 1577–1599, doi:[10.1175/2546.1](https://doi.org/10.1175/2546.1).
- , M. L. Black, S. S. Chen, and R. A. Black, 2007: An evaluation of microphysics fields from mesoscale model simulations of tropical cyclones. Part I: Comparisons with observations. *J. Atmos. Sci.*, **64**, 1811–1834, doi:[10.1175/JAS3932.1](https://doi.org/10.1175/JAS3932.1).
- Schubert, W. H., and J. J. Hack, 1982: Inertial stability and tropical cyclone development. *J. Atmos. Sci.*, **39**, 1687–1697, doi:[10.1175/1520-0469\(1982\)039<1687:ISATCD>2.0.CO;2](https://doi.org/10.1175/1520-0469(1982)039<1687:ISATCD>2.0.CO;2).
- Shapiro, L. J., and H. E. Willoughby, 1982: The response of balanced hurricanes to local sources of heat and momentum. *J. Atmos. Sci.*, **39**, 378–394, doi:[10.1175/1520-0469\(1982\)039<0378:TROBHT>2.0.CO;2](https://doi.org/10.1175/1520-0469(1982)039<0378:TROBHT>2.0.CO;2).
- Shelton, K. L., and J. Molinari, 2009: Life of a six-hour hurricane. *Mon. Wea. Rev.*, **137**, 51–67, doi:[10.1175/2008MWR2472.1](https://doi.org/10.1175/2008MWR2472.1).
- Shieh, O. H., M. Fiorino, M. E. Kucas, and B. Wang, 2013: Extreme rapid intensification of Typhoon Vicente (2012) in the South China Sea. *Wea. Forecasting*, **28**, 1578–1587, doi:[10.1175/WAF-D-13-00076.1](https://doi.org/10.1175/WAF-D-13-00076.1).
- Shu, S., J. Ming, and P. Chi, 2012: Large-scale characteristics and probability of rapidly intensifying tropical cyclones in the western North Pacific basin. *Wea. Forecasting*, **27**, 411–423, doi:[10.1175/WAF-D-11-00042.1](https://doi.org/10.1175/WAF-D-11-00042.1).
- Sitkowski, M., and G. M. Barnes, 2009: Low-level thermodynamic, kinematic, and reflectivity fields of Hurricane Guillermo (1997) during rapid intensification. *Mon. Wea. Rev.*, **137**, 645–663, doi:[10.1175/2008MWR2531.1](https://doi.org/10.1175/2008MWR2531.1).
- Skamarock, W. C., and Coauthors, 2008: A description of the Advanced Research WRF version 3. NCAR Tech. Note NCAR/TN-475+STR, 113 pp., doi:[10.5065/D68S4MVH](https://doi.org/10.5065/D68S4MVH).
- Stern, D. P., J. L. Vigh, D. S. Nolan, and F. Zhang, 2015: Revisiting the relationship between eyewall contraction and intensification. *J. Atmos. Sci.*, **72**, 1283–1306, doi:[10.1175/JAS-D-14-0261.1](https://doi.org/10.1175/JAS-D-14-0261.1).
- Stevenson, S. N., K. L. Corbosiero, and J. Molinari, 2014: The convective evolution and rapid intensification of Hurricane Earl (2010). *Mon. Wea. Rev.*, **142**, 4364–4380, doi:[10.1175/MWR-D-14-00078.1](https://doi.org/10.1175/MWR-D-14-00078.1).
- Tang, B., and K. Emanuel, 2010: Midlevel ventilation's constraint on tropical cyclone intensity. *J. Atmos. Sci.*, **67**, 1817–1830, doi:[10.1175/2010JAS3318.1](https://doi.org/10.1175/2010JAS3318.1).
- Tao, W.-K., and J. Simpson, 1993: The Goddard cumulus ensemble model. Part I: Model description. *Terr. Atmos. Oceanic Sci.*, **4**, 35–72.

- Vigh, J. L., and W. H. Schubert, 2009: Rapid development of the tropical cyclone warm core. *J. Atmos. Sci.*, **66**, 3335–3350, doi:[10.1175/2009JAS3092.1](https://doi.org/10.1175/2009JAS3092.1).
- Wang, H., and Y. Wang, 2014: A numerical study of Typhoon Megi (2010). Part I: Rapid intensification. *Mon. Wea. Rev.*, **142**, 29–48, doi:[10.1175/MWR-D-13-00070.1](https://doi.org/10.1175/MWR-D-13-00070.1).
- Wang, Y., 2007: A multiply nested, movable mesh, fully compressible, nonhydrostatic tropical cyclone model—TCM4: Model description and development of asymmetries without explicit asymmetric forcing. *Meteor. Atmos. Phys.*, **97**, 93–116, doi:[10.1007/s00703-006-0246-z](https://doi.org/10.1007/s00703-006-0246-z).
- , and G. J. Holland, 1996: Tropical cyclone motion and evolution in vertical shear. *J. Atmos. Sci.*, **53**, 3313–3332, doi:[10.1175/1520-0469\(1996\)053<3313:TCMAEI>2.0.CO;2](https://doi.org/10.1175/1520-0469(1996)053<3313:TCMAEI>2.0.CO;2).
- , Y. Rao, Z.-M. Tan, and D. Schönemann, 2015: A statistical analysis of the effects of vertical wind shear on tropical cyclone intensity change over the western North Pacific. *Mon. Wea. Rev.*, **143**, 3434–3453, doi:[10.1175/MWR-D-15-0049.1](https://doi.org/10.1175/MWR-D-15-0049.1).
- Willis, P. T., and D. P. Jorgensen, 1981: Reflectivity relationships for hurricanes. Preprints, *20th Conf. on Radar Meteorology*, Boston, MA, Amer. Meteor. Soc., 85–90.
- Xu, J., and Y. Wang, 2015: A statistical analysis on the dependence of tropical cyclone intensification rate on the storm intensity and size in the North Atlantic. *Wea. Forecasting*, **30**, 692–701, doi:[10.1175/WAF-D-14-00141.1](https://doi.org/10.1175/WAF-D-14-00141.1).
- Xu, Y., and Y. Wang, 2013: On the initial development of asymmetric vertical motion and horizontal relative flow in a mature tropical cyclone embedded in environmental vertical shear. *J. Atmos. Sci.*, **70**, 3471–3491, doi:[10.1175/JAS-D-12-0335.1](https://doi.org/10.1175/JAS-D-12-0335.1).
- Zeng, Z., Y. Wang, and L. Chen, 2010: A statistical analysis of vertical shear effect on tropical cyclone intensity change in the North Atlantic. *Geophys. Res. Lett.*, **37**, L02802, doi:[10.1029/2009GL041788](https://doi.org/10.1029/2009GL041788).
- Zhang, F., and D. Tao, 2013: Effects of vertical wind shear on the predictability of tropical cyclones. *J. Atmos. Sci.*, **70**, 975–983, doi:[10.1175/JAS-D-12-0133.1](https://doi.org/10.1175/JAS-D-12-0133.1).